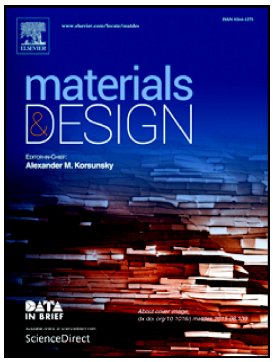

Manufacturability, mechanical properties, mass-transport properties and biocompatibility of TPMS scaffolds fabricated by selective laser melting

Shuai Ma, Qian Tang, Xiaoxiao Han, Qixiang Feng, Jun Song, Rossitza Setchi, Ying Liu, Yang Liu, Athanasios Goulas, Daniel S. Engstrøm, Yau Yau Tse, Ni Zhen

PII: S0264-1275(20)30569-4

DOI: https://doi.org/10.1016/j.matdes.2020.109034

Reference: JMADE 109034

To appear in: *Materials & Design*

Received date: 17 April 2020

Revised date: 29 June 2020

Accepted date: 3 August 2020

Please cite this article as: S. Ma, Q. Tang, X. Han, et al., Manufacturability, mechanical properties, mass-transport properties and biocompatibility of TPMS scaffolds fabricated by selective laser melting, *Materials & Design* (2020), https://doi.org/10.1016/j.matdes.2020.109034

Manufacturability, Mechanical Properties, Mass-Transport Properties and Biocompatibility of TPMS Scaffolds Fabricated by Selective Laser Melting

Shuai Ma[1], Qian Tang[1*], Xiaoxiao Han[2*], Qixiang Feng[1], Jun Song[1], Rossitza Setchi[3], Ying Liu[3], Yang Liu[4], Athanasios Goulas[4], Daniel S.Engstrøm[4], Yau Yau Tse[5], Ni Zhen[4]

[1] State Key Laboratory of Mechanical Transmissions, Chongqing University, Chongqing, China, 400044

[2] State Key Laboratory of Advanced Design and Manufacturing for Vehicle Body, Hunan University, China, 410082

[3] Cardiff School of Engineering, Cardiff University, Cardiff, UK, CF24 3AA

[4] Wolfson School of Mechanical, Electrical and Manufacturing Engineering, Loughborough University, Loughborough, UK, LE11 3TU

[5] Department of Materials, Loughborough University, Loughborough, UK, LE11 3TU

* Corresponding author

Abstract

Selective laser melting is a promising additive manufacturing technology for manufacturing porous metallic bone scaffolds. Bone repair requires scaffolds that meet various mechanical and biological requirements. This paper addresses this challenge by comprehensively studying the performance of porous scaffolds. The main novelty is exploring scaffolds with different porosities, verifying various aspects of their performance and revealing the effect of their permeability on cell growth. This study evaluates the manufacturability, mechanical behaviour, permeability and biocompatibility of gyroid scaffolds. In simulations, mechanical behaviour and permeability exhibited up to 56% and 73% accuracy, respectively, compared to the experimental data. The compression and permeability experiments showed that the elastic modulus and the permeability of the scaffolds were both in the range of human bones. The morphological experiment showed that manufacturing accuracy increased with greater designed porosity, while the in vitro experiments revealed that permeability played the main role in cell proliferation. The significance of this work is improving the understanding of the effect of design parameters on the mechanical properties, permeability and cell growth of the scaffolds, which will enable the design of porous bone scaffolds with better bone-repair effects.

Keywords: Selective Laser Melting; Bone Scaffold; Biocompatibility; Mechanical Behaviour; Transmission Properties

1. Introduction

Additive manufacturing (AM) is a promising research technology in bone repair. Through the use of three-dimensional (3D) models directly obtained by computerised tomography scans of bones, AM allows bone replacements using customised bone scaffolds with the same shapes as the damaged bones of patients. Tissue engineering uses several biocompatible materials, such as Ti6Al4V [1], polycaprolactone-hydroxyapatite [2] and 316L stainless steel [3]. Compared to polymeric materials [4], metal materials have higher strength, better corrosion resistance and stronger cell adhesion, and 316L stainless steel in particular enjoys wide use to fabricate bone scaffolds due to its superior corrosion prevention, biocompatibility and low cost [3, 5]. Selective laser melting (SLM) is a preferred AM method for metallic bone scaffolds because it can produce well-defined structure borders [6] using a variety of metal powders, such as Ti6Al4V, 316L stainless steel, Fe-Mn and Zn. [7-11]. More importantly, SLM allows the design and fabrication of porous structures to fill the interior of the scaffold, especially those with triply periodic minimal surfaces (TPMSs), which are supposed to enhance bone repair [12, 13]. Therefore, 316L stainless steel TPMS scaffolds were fabricated by SLM in this study.

TPMS structures have many advantages in bone scaffold design; their parameters, such as pore size and porosity, can be easily adjusted by control equations to tailor the mechanical properties of metallic scaffolds to be more like those of bones [14]. TPMS structures can also lead to effective fixation through optimised interfacial resistance, which is caused by the integration of the scaffold and bone tissue [15, 16]. In addition, TPMS can provide micropores; notably, Barba et al. concluded that a 300–600 μm pore size is better for osseointegration since it benefited vascularisation and cell growth [17]. Moreover, TPMS structures provide a large area in which cells can grow. Thus, TPMS bone scaffolds are a promising field of research.

The design of TPMS scaffolds must be explored and verified to meet the multiple requirements of bone repair. The four most important characteristics of bone scaffolds

are manufacturability, biocompatibility, mechanical properties and permeability [18-21]. These characteristics relate to scaffolds' repeatability, their ability to bear loads and their exchange of nutrients, which can influence the effects of bone repair. These characteristics mainly depend on the porosity, pore size, cell unit and geometry of the structures [22-24]. Previous literature has focused more on the effects of porous structures' parameters on a single requirement [25, 26]. However, these results were difficult to combine to verify effectively whether the design parameters met the multiple requirements in bone-repair process, as the parameters and design method for the bone scaffolds that were studied were inconsistent. Therefore, systematically studying and evaluating these characteristics under consistent design standards is important, considering that bone repair is complex. To design a scaffold to meet multiple requirements, reasonable parameters can only be chosen if their influence on each property is comprehensively considered.

Previous research has reported the advantages and effects of using various TPMS structures. For example, TPMS can avoid stress concentration and have smooth-transition stress distribution due to its continuously curved surface [27, 28]. The control equations of TPMS can be adjusted as the coordinates change to obtain smooth and continuous curved surfaces [29]. Moreover, TPMSs are suitable for graded design [30]. Montazerian et al. compared four kinds of TPMS with uniform porosity and graded porosity; the results indicated that graded design structures can reach greater permeabilities and better mechanical properties due to a radially gradient porosity distribution [31]. As one type of TPMS structure, a gyroid structure has self-supported features and excellent mechanical properties [32, 33]. Du Plessis et al. compared traditional strut-based structures with minimal surface structures and concluded that a gyroid structure was one of the best design structures due to its combination of porosity and permeability [34]. Notably, the topology of a structure affects manufacturing precision, and the gyroid structure had greater accuracy than other porous structures, such as the Schwarz Diamond structure [17]. Thus, a gyroid structure was selected as the representative TPMS in this study.

Roughness is an indicator of quality, as a rough surface significantly benefits cell differentiation and growth, and can also lead to stress localisation [35]. The surfaces of SLM-built parts are usually rough due to residual powder and the use of layer-by-layer scanning methods. Arash et al. designed three kinds of gyroid

structures, and the roughness of the structures Ra were reported to range from 3–5 μm [36]. Post-processing, such as grinding and electrolytic processing, can smooth their surfaces and even obtain a Ra of ~0.13 μm [37]. Faia-Torres et al. designed a surface roughness gradient sample with roughness from ~0.5–4.7 μm; their cell cultures indicated that cell growth increased with greater Ra [38]. In addition, scaffolds with suitable roughness can enhance the attraction of cells for bone formation [39], and a rough surface can provide more surface area than can a smooth one. Roughness can also affect the corrosion resistance of scaffolds, which ensures biocompatibility [40]. Porosity is an important parameter for bone scaffolds because it can affect both mechanical properties and permeability. The literature has suggested that the porosity values of as-built parts are generally lower than their designed values [41]. Thus, the accuracy of porosity can be considered another indicator of quality, as the accuracy of different porosities in scaffolds may vary [25, 26]. Arabnejad et al. adjusted the strut thickness while maintaining pore size to obtain various porosity scaffolds. They reached a good consistency with the designed value when the scaffolds had low designed porosity, but the porosity accuracy was limited, and the manufacturing error rate reached 15% when the designed porosity was 75% [42]. New design methods to enhance the porosity accuracy of high-porosity scaffolds require further investigation. Previous literature has reported relative densities (RDs) of 96–99% from parts made using SLM of 316L [43-46]. Therefore, the RD of gyroid structures must be investigated to evaluate their quality and manufacturability.

Suitable mechanical properties are a basic requirement for a scaffold: there should be an elastic modulus that is similar to that of the host bone to avoid the ‘stress shielding effect’, meaning the load is mainly borne by the scaffold, which can lead to osteoporosis [17]. While compression experiments can investigate the elastic moduli of porous scaffolds, they increase design time and costs. Thus, computer simulations are necessary to predict the performance of porous structures. Some studies have used simulations to evaluate the mechanical behaviours of lattice structures [47]. It has been reported that, compared to strut structures, such as the body-centred cubic structure, TPMSs struggle to achieve perfect agreement with the experiments due to their complex structures, incomplete melting of powders and internal pores [48, 49]. Harrysson et al. reported that the ratio of elastic modulus experimental results to simulation results ranged from 10.6–14.8% [50], although Hazlehurst et al. reported ~33%. [51]. Bill et al. introduced elliptical cross-sections to mimic manufactured

struct geometry to improve simulation accuracy [52]. However, the reasons for the difference between the experiments and the simulations were not clear. To investigate the possibility of predicting the mechanical properties of gyroid structures and the possible reasons for simulation errors, a compression experiment, a finite element analysis (FEA) and a relative density experiment were conducted in this study.

Permeability must be considered when designing a scaffold because it can affect cell metabolism, the mass transport of nutrients and oxygen and cell migration [18]. The permeability of a bone scaffold is affected by its porosity, pore size and structure type. Predicting a scaffold's permeability at the design stage is necessary to ensure that it is in the permeability range of human bones. Some scholars have analysed the permeability of various structures via simulations or experiments. Zhang et al. investigated the permeability of graded Ti-6Al-4V scaffolds, and the results showed that the graded scaffold was in the permeability range of human bones [53]. Computational fluid dynamics (CFD) was widely used for microscale flows [54], Ali studied the permeability of gyroid and lattice scaffolds by CFD and compared the CFD results with the experimental results of other scholars, finding that the 80% porosity of the gyroid structure was the optimum permeability structure [55]. However, the effect of permeability on cell-growth needs and the predictability and causes of permeability simulation errors require further study. For this permeability test, CFD and a cell-culture experiment were combined.

Although TPMS structures were found suitable for bone scaffold design in some respects, to enhance bone-repair efficiency, the porous structure of bone scaffolds requires additional exploration. The aims of this study are to further investigate the effects of porous structures' parameters on the properties of scaffolds from multiple perspectives and to explore the possibility that a porous structure can meet multiple needs simultaneously. The novelty of this study is in verifying that gyroid scaffolds can meet the needs of bone repair in different situations. To these ends, this study evaluates the manufacturability and investigates the effects of parameters on the mechanical and transport properties of gyroid scaffolds. It then introduces cell-culture experiments to reveal the influence of permeability on cell growth. The study also introduces simulations to evaluate the predictability of the mechanical and transport properties of the scaffolds. This study is significant because it offers useful advice on scaffold design and the choice of suitable parameters by considering multiple

requirements to achieve desirable bone-repair effects.

2. Methodology

2.1 Modelling and simulation

2.1.1 Design of 316L gyroid scaffolds

To obtain uniform distributed pore sizes, the gyroid structure was determined by the following equation [56]:

$$\sin\frac{2\pi x}{L}\cos\frac{2\pi y}{L}+\sin\frac{2\pi y}{L}\cos\frac{2\pi z}{L}+\cos\frac{2\pi x}{L}\sin\frac{2\pi z}{L}=0 \qquad \text{(Eq. 1)}$$

In the above equation, L is the length of the cube in which the porous unit was located. To model and modify the structures easily, the key characteristic curves in the x = L/2 (see (Eq. 2)) and z = L/4 (see (Eq. 3)) planes were modelled by Creo software through parametric equations.

$$\begin{cases} x = \frac{L}{2} \\ y = \theta \times \frac{L}{2} \\ z = \frac{\arctan(\sin\pi\theta)\times\frac{L}{2}}{\pi} - \frac{L}{2} \end{cases} \quad (\theta \in (0,1)) \qquad \text{(Eq. 2)}$$

$$\begin{cases} z = \frac{L}{4} \\ x = -\frac{L}{2} + L \times \theta \\ y = \frac{\arctan\left(-\sin\left(\theta\times 2\pi+\frac{\pi}{2}\right)\right)\times\frac{L}{2}}{\pi} \end{cases} \quad (\theta \in (0,1)) \qquad \text{(Eq. 3)}$$

where θ is a variable to determine the 3D coordinates of the points on the key characteristic curves. As Fig. 1 (a) shows, the other characteristic curves in the x = -L/2 and ± L/4, y = ± L/2 and ± L/4, and z = ± L/2 and – L/4 planes could be modelled by a similar equation. We then generated a surface within the closed curve consisting of all the characteristic curves. The structure's solid 3D model was obtained by thickening along the normal direction of the surface. As Fig. 1 (b) shows, the design method kept the thickness of all the models the same and defined different lengths of the unit to model different porosities' structures. The thickness in this study was 0.1 mm, and five gyroid structures with porosities ranging from 75.1% to 88.8% were designed. The scaffolds for the cell culture included 6.5-mm diameter cylinders that were 6 mm in height; to calculate the strain simply, five kinds of samples for the

compression experiment included 6.5-mm diameter cylinders that were 10 mm in height. In all, ten kinds of models were built, and four workpieces were fabricated for each model via SLM. Table 1 shows the details of the ten models. Samples C05–C13 were used in the cell culture experiment, and samples G05–G13 were used in the compression test.

Table 1 Characteristics of gyroid scaffolds computer aided design (CAD) models

Sample	Pore size (μm)	Porosity (%)	Diameter (mm)	Height (mm)	Surface area (mm^2)	Volume (mm^3)	Sa/vol (mm^{-1})
C05	500	75.1	6.5	6	1042.4	48.5	21.5
C07	700	81.7	6.5	6	819.1	37.6	21.8
C09	900	84.6	6.5	6	656.7	30.2	21.8
C11	1100	87.2	6.5	6	542.6	24.8	21.9
C13	1300	88.8	6.5	6	476.0	22.5	21.2
G05	500	75.1	6.5	10	1727.6	80.7	21.4
G07	700	81.7	6.5	10	1357.0	62.8	21.6
G09	900	84.6	6.5	10	1089.3	50.1	21.7
G11	1100	87.2	6.5	10	903.2	41.5	21.8
G13	1300	88.8	6.5	10	794.4	36.6	21.7

2.1.2 Modelling and quasi-static simulation method of gyroid structures

Abaqus software was used to predict the elastic modulus and yield strength of each kind of scaffold, and quasi-static analysis was introduced in this simulation [49]. To simulate the compression experiment, the simulated model of mechanical properties was established (see Fig. 1 (c)). The model consisted of 2 × 2 × 2 gyroid units. A rigid surface was then set at the top of the sample with a displacement of 0.8 mm, and another rigid surface was fixed at the bottom of the sample as the platform of the compression experiment. The material was 316L stainless steel with a 7.87 g/cm^3 density, 117,000 MPa Young's modulus, 0.3 Poisson's ratio, and 380 MPa yield stress (the data were provided by the powder supply company: LPW Technology Ltd.). The models were meshed by free-grid technology. Table 2 shows the element types and number of elements. The force and displacement data of the sample were obtained

from a reference point on the moving rigid surface.

Table 2 The element types and number of elements for the FEA and CFD models (C3D4 = 4-node linear tetrahedral element, F = fluid)

	Element type	Number of elements				
		G05	G07	G09	G11	G13
FEA	C3D4	96377	84837	104691	148362	194735
CFD	FC3D4	279729	279323	246458	252120	299389

2.1.3 Modelling of mass transport

In this study, CFD was used to simulate the process of transmission obeying the Navier-Stokes equation (Eq. 4) and then calculate the permeability of each model. Next, the relationship between porosity (pore size) and permeability was obtained.

Fig. 1 (e) shows the modelling and boundary-condition setting for the CFD analysis, and Table 2 shows the element types and number of elements. The first step was to model a porous 3D scaffold model, which consisted of 2 × 2 × 2 units. Next, a rectangular fluid domain was built, and a Boolean operation was used with the previous 3D scaffold model; the fluid domain of the scaffold was then retrieved. To avoid the boundary effect caused by the inlet area, a virtual fluid domain was built. The flow direction of the fluid at the inlet was vertical, and the velocity was 0.1 mm/s [55, 57]. To calculate the pressure drop from the top surface to the bottom surface of the scaffold conveniently, the pressure of the outlet was set to 0 Pa; ΔP represents the average pressure of the top surface. The inside surface in the fluid domain, which was produced by the Boolean operation, was set as the wall boundary, and the outside surface of the fluid domain in the vertical direction was set as the symmetric boundary. In this simulation, water was chosen as the fluid with a density of 1 g/mm^3 and a viscosity of 1.01 × 10^{-9} MPa·s. The pore size D of the gyroid unit was used to calculate the Reynolds number (Eq. 5), and then the laminar was confirmed by judging whether the Reynolds number was $1 < Re < 10$ [58]. Darcy's law (Eq. 6) was used to determine the permeability of the scaffold.

$$\rho\frac{\partial \mathbf{v}}{\partial t} = -(\mathbf{v}\cdot\nabla)\mathbf{v} - \frac{1}{\rho}\nabla P + \mu\nabla^2\mathbf{v} + F \quad \text{(Eq. 4)}$$

$$Re = \frac{v\cdot\rho\cdot D}{\mu} \quad \text{(Eq. 5)}$$

$$k = \frac{v\cdot\mu\cdot L}{\Delta P} \quad \text{(Eq. 6)}$$

where

- ρ is the density of the fluid (g/cm^3)
- **v** is the velocity of the water (mm/s)
- t is time (s)
- **∇** is the delta operator (-)
- P is pressure (MPa)
- μ is the dynamic viscosity coefficient of the fluid (MPa·s)
- F is the force (N)
- Re is the Reynolds number (-)
- D is the diameter of the pore (mm)
- K is the permeability coefficient (mm^2)
- ΔP is the pressure difference (MPa)

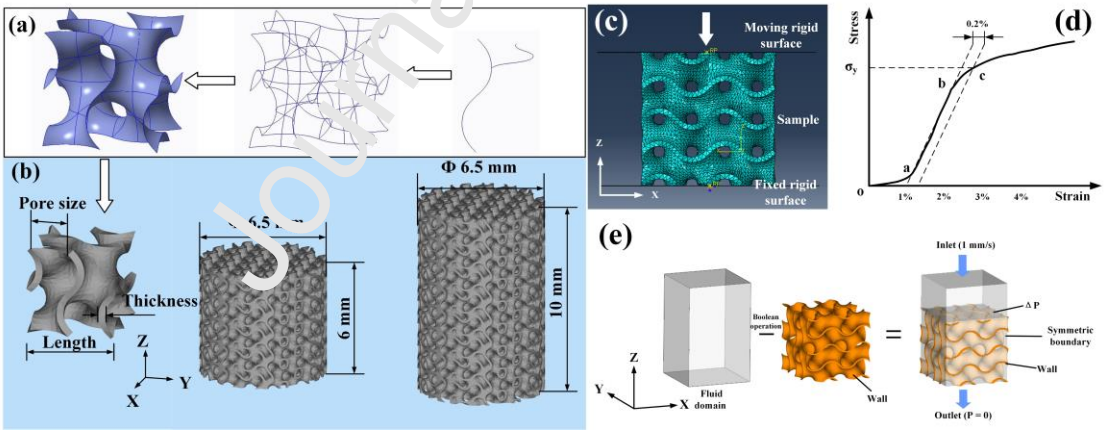

Fig. 1 (a) Modelling process of gyroid structure. (b) Unit of gyroid structure (left), sample for cell culture (middle) and sample for compression experimental test (right). (c) Boundary conditions of the compression simulation. (d) Schematic of strain-stress curve, elastic modulus and yield strength. (e) Modelling process of fluid domain and setting the boundary conditions of CFD analysis.

2.2 Experiments

2.2.1 Powder characteristics and additive manufacturing of TPMS scaffolds

All the samples were fabricated using gas-atomised 316L stainless steel powders (LPW Technology Ltd., Runcorn, Cheshire, UK) of 7.87 g/cm^3 density with a chemical composition of C ≤ 0.03%; Cr 17.5–18.00%; Cu ≤ 0.5%; Fe – bal.; and a particle size range of 15–45 μm. The morphology and particle size distribution of the feedstock powder were verified using laser diffraction (Mastersizer Scirocco 2000, Malvern Instruments Ltd., Malvern, UK) and a field emission scanning electron microscope (FESEM) (7100, Jeol Ltd., Japan).

Fig. 2 (a) shows the size distribution curve of the 316L powders; the curve shows good symmetry. The peak point of the curve means that the peak particle size is about 30.20 μm, the corresponding volume of which is 17.32%. A scanning electron microscope (SEM) was used to observe the microtopography of the powders, as Fig. 2 (b) shows. Many particles were spherical and were consistent with the results of the particle size analysis.

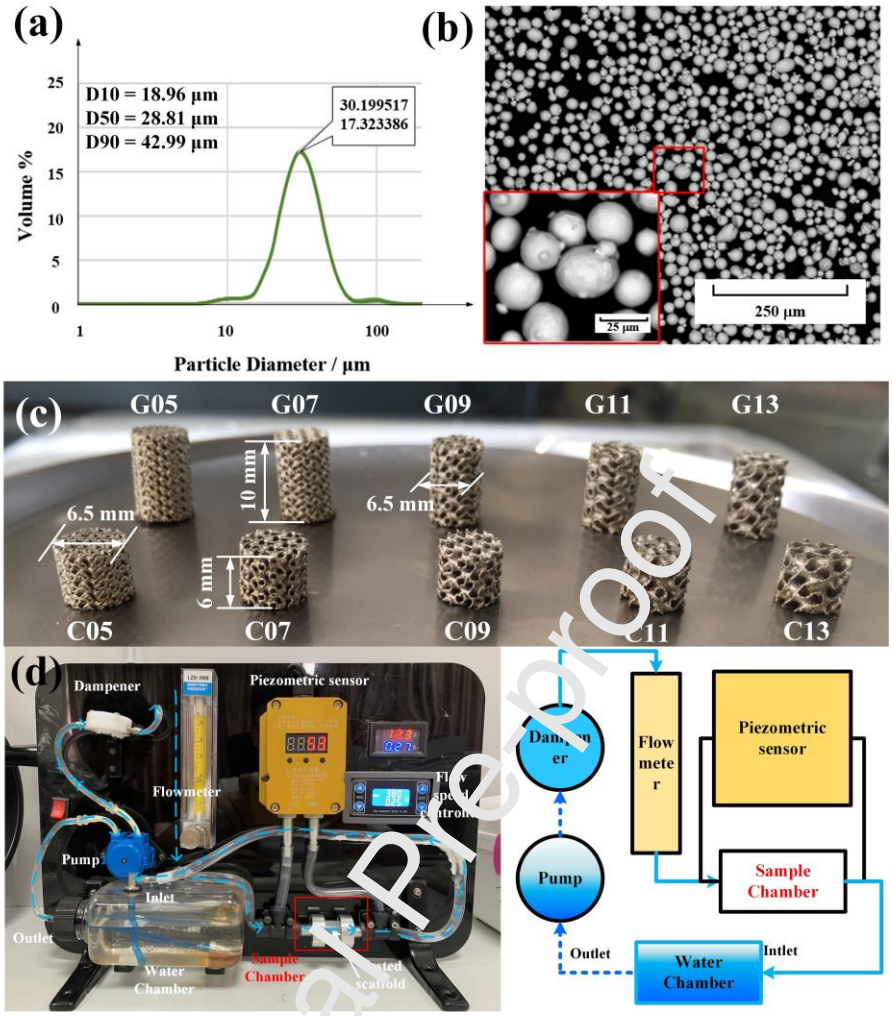

Fig. 2 (a) The particle size distribution curve of 316L powders. (b) SEM images of 316L stainless steel. (c) SLM-built samples. (d) Test bed (left) and schematic diagram (right) of permeability experiment (rate of flow 40, 60 and 80 ml/min).

All the SLM experimentation and manufacturing of the test specimens in this study were carried out on an SLM machine (SLM100A, Realizer GmbH, Borchen, Germany) and built along the z-axis. The SLM100A was equipped with a continuous wave ytterbium-doped fibre laser (YLR-50, IPG Photonics, Oxford, MA, USA) operating on a central emission wavelength of λ = 1.06 mm with a standard TEM00 Gaussian beam profile and a maximum indicated power output of 50 W. The SLM100A was equipped with an adjustable beam expander that could deliver a focused beam 30–300 µm in diameter onto the powder bed through a 120-mm f-theta lens. A combination of 50-W laser power, 150-µm laser exposure time and 30-µm point distance led to a 200-mm/s scanning speed and 50-µm hatch spacing. The beam expander was set at 14.50 mm, producing a 50-µm laser beam spot. Each layer was

scanned once, with a 90° change in scanning direction per layer. No skin hatch strategy or heating on the build platform was used. The above-mentioned processing parameters were provided by the SLM equipment manufacturer based on the powder feedstock.

The samples shown in Fig. 2 (c) were separated from the substrate by wire electrical discharge machining and were finally formed into the target size. To remove the remaining powder from the surfaces of the samples, all the samples were cleaned by an ultrasonic cleaner immersed in isopropanol for 5 min, and the samples were not subjected to any other post-treatment or heat treatment after washing.

2.2.2 Morphological analysis

To judge the manufacturing accuracy of the porosity, the density method was used to calculate the porosity of SLM-built scaffolds, as the equations below show:

$$\Phi = \left(1 - \frac{\rho_p}{\rho_s}\right) \times 100\% \quad \text{(Eq. 7)}$$

$$\rho_p = \frac{m_p}{v_p} \quad \text{(Eq. 8)}$$

$$v_p = \pi h \left(\frac{Dp}{2}\right)^2 \quad \text{(Eq. 9)}$$

$$\Phi = \left(1 - \frac{m_p}{m_s}\right) \times 100\% \quad \text{(Eq. 10)}$$

where

- Φ is the porosity (%)
- ρ_p is the density of the porous material (g/mm^3)
- ρ_s is the density of the solid material (g/mm^3)
- m_p is the mass of the porous sample (g)
- v_p is the volume of the cylinder (mm^3)
- h is the height of the sample (mm)
- D_p is the diameter of the cylinder (mm)
- m_s is the mass of the solid material with the same volume as the porous sample (g)

The height, diameter and mass of each sample were measured, and then the as-built

porosity was measured. Next, the error between as-built porosity and designed porosity was calculated. The manufactured error of porosity was calculated by the following equation:

$$e_P = (\Phi_D - \Phi_P) \times 100\% \quad \text{(Eq. 11)}$$

where Φ_p is the porosity of the as-built sample and Φ_D is the designed porosity. In addition, a specific gravity balance (HZY-A120, USA, 0.001g, 23 ℃) was used to measure the relative density and was calculated based on the Archimedes method.

An optical microscope (OM) (VHX-1000 digital microscope) was used to measure the external thickness T of each sample, and each sample was measured eight times at a random area on the top surface. Then the pore size D_{pore} was calculated by (Eq. 12), where L is the length of the unit.

$$D_{pore} = \frac{L}{2} - T \quad \text{(Eq. 12)}$$

A 3D confocal microscopy (LEXT OLS4100, Olympus, Japan) was used to measure the roughness of the top, side and bottom surfaces of the as-built sample. For each surface, four randomly selected spots (642 × 644 μm) were tested. In each spot, the roughness was measured three times in both the horizontal and vertical directions; the mean values were then reported. Meanwhile, the microscopic morphology of the scaffold surface was also observed by confocal microscopy. To analyse the internal thickness, as-built porosity and internal pores of scaffolds, a micro-computed tomography (CT) scanner (d2, Diondo, Germany) was used to scan G05–G13 at 100KV voltage and 5 μm resolution. Finally, the CAD data was compared to the CT data to study the manufactured deviation.

2.2.3 Compression tests

A universal testing machine was used to investigate the mechanical properties of the 316L stainless steel gyroid scaffolds. There was no lubrication between the upper and lower crossheads, and the lateral expansion was not restricted. The loading force was loaded on the top surfaces of the samples along the z-axis, where the height of the compression samples was 10 mm; a slow speed of 1 mm/min was used in the experiment to record the displacement and reaction force of the crosshead and calculate the strain-stress curve by the following equation:

$$\sigma = \frac{F}{A} \quad \text{(Eq. 13)}$$

$$\varepsilon = \frac{\Delta h}{h} \quad \text{(Eq. 14)}$$

where

- σ is stress (MPa)
- F is the reaction force of the crosshead (N)
- A is the cross-sectional area of the equivalent cylinder, the cross-section being perpendicular to the z-axis (mm^2)
- Δh is the displacement of the upper crosshead (mm)
- h is the height of the test sample (mm)
- ε is a strain (%)

As Fig. 1 (d) shows, line a–b is the elastic deformation stage, the slope of which is the elastic modulus of each scaffold. The 316L stainless steel scaffolds did not appear to have an obvious yield point, and the stress of the 0.2% residual deformation point was the offset yield stress σ_y. Three specimens of each sample (G05–G13) were used in the compression experiment.

2.2.4 Permeability experiment

The experimental permeability test was set to compare with the simulated results. As Fig. 2 (d) shows, a pump and dampener were used to provide a steady flow, and a speed controller was also used to adjust the flow rate. A pressure sensor was set between the inlet and outlet of the sample chamber to measure the pressure difference, and the flow rate was measured by a column flowmeter. The pressure difference of the sample chamber $\Delta P_{chamber}$ without a scaffold was measured first and then subtracted from the total pressure ΔP_{total}. The pressure drop of the scaffold $\Delta P_{scaffold}$ was calculated using (Eq. 15). All the samples were tested at the flow rates of 40, 50, 60, 70, 80 and 90 mL/min. The experiment was repeated five times with each sample under different flow rates; the results were expressed in terms of mean and standard deviation, and then they were compared with the simulation results.

$$\Delta P_{scaffold} = \Delta P_{total} - \Delta P_{chamber} \quad \text{(Eq. 15)}$$

2.2.5 Cell-culture experiment

To research the influences of pore size and scaffold porosity on cell growth, bone cell–culture experiments were performed for 3 and 7 days. For each time point, two specimens were required for each porosity scaffold to calculate the cell numbers and observe the morphology, respectively. For this, four experiment groups named A, B, C and D were set up, as shown in Table 3. Groups A and B were planned to culture for 3 days and groups C and D for 7 days; samples from groups A and C were used to count the cells and groups B and D to observe the morphology of the cells. Each group had five kinds of scaffolds with one sample for each scaffold, and a blank control group was set in groups A and C.

Table 3 Experimental grouping and notes of cell-culture experiment

Pore Size (μm)	500	700	900	1100	1300	Blank Control	Notes
Group A	C05A	C07A	C09A	C11A	C13A	BCA	3-day, cell count
Group B	C05B	C07B	C09B	C11B	C13B	-	3-day, cell fixation
Group C	C05C	C07C	C09C	C11C	C13C	BCC	7-day, cell count
Group D	C05D	C07D	C09D	C11D	C13D	-	7dany, cell fixation

All the as-built scaffolds for the cell cultures were cleaned in isopropanol through the ultrasonic cleaner three times for 5 min for each to remove the residual powder in the pores and semi-melted powder at the surface. All the samples were then placed in a 24-well plate. To sterilise the scaffolds, sterile water was used to wash the samples three times after two h of soaking in acetone in the well. Human Caucasian osteosarcoma, TE85 (ECACC No. 87070202), was used, and 4×10^5 cells were placed in each well and cultured in the cell culture medium Dulbecco's modified eagle medium, which consisted of 10% fetal bovine serum, and 1% L-Glutamine; the medium was refreshed every three days. Before the cells were counted, all the samples were transferred to a new 24-well plate. Then, 1 ml of TrypLE Express was

added to both the old and new 24-pore plates, and they were placed in an incubator for 5 min. To ensure that all the cells were detached from the surface of the scaffold and fell into the solution, 1 ml of fresh medium was added to each well to wash the samples. All the solutions in each well were collected and centrifuged for 5 min at 0.3 G to remove the supernatant. After that, 0.19 ml of fresh medium and 0.01 ml of dye were used to resuspend the cells. The automated cell-counting system of a NucleoCounter machine (NC-3000) was used to count all the cells on each scaffold; the number of cells per unit area was then calculated. Table 1 shows the surface area of each scaffold. The scaffolds in groups B and D were transferred to a new 24-well plate before fixation, and all the scaffolds were washed by phosphate buffered saline, and paraformaldehyde was then added to each well as the fixation buffer at room temperature. All the samples were washed with sterile water three times after 20 min of fixation. After fixation, samples from 3 (Group B) and 7 (Group D) days of cell culture were dehydrated with a series of ethanol solutions, and the cells on the surface of each scaffold were observed using a FESEM (7100, JEOL Ltd., Japan).

3. Results

3.1 Morphology of scaffolds

The mass of each sample was measured by an electric balance after removing the remaining powder in an ultrasonic bath, and then the porosity was calculated by (Eq. 10). The porosities of the as-built samples were calculated from four duplicate samples of each type of scaffold; Fig. 3 (a) shows the results. The designed porosities of G05–G13 ranged from 75.1–88.8%, while the manufactured porosities (measured by density method) ranged from 50.5–81.9%. The as-built porosity measured by the CT experiment agreed well with the density method. All manufactured porosities were lower than the designed porosity of each type of scaffold. The error between designed and manufactured porosity decreased as the designed porosity increased; the minimum manufactured error was 6.9% when the designed porosity was 88.8%. Fig. 3 (b) shows the manufactured error of each as-built sample grouped by designed porosity from G05–G13. The manufactured errors remained consistent in each group. The difference between the maximum and minimum in each group ranged from 1.61–4.90%, and it should be noted that the difference decreased as the manufactured error decreased. When the designed porosity was greater than 84.6% (pore size 900 μm, G09), the manufacturing stability greatly improved. The above results show that, with

greater designed porosity, manufacturing errors decrease and manufacturing stability improves.

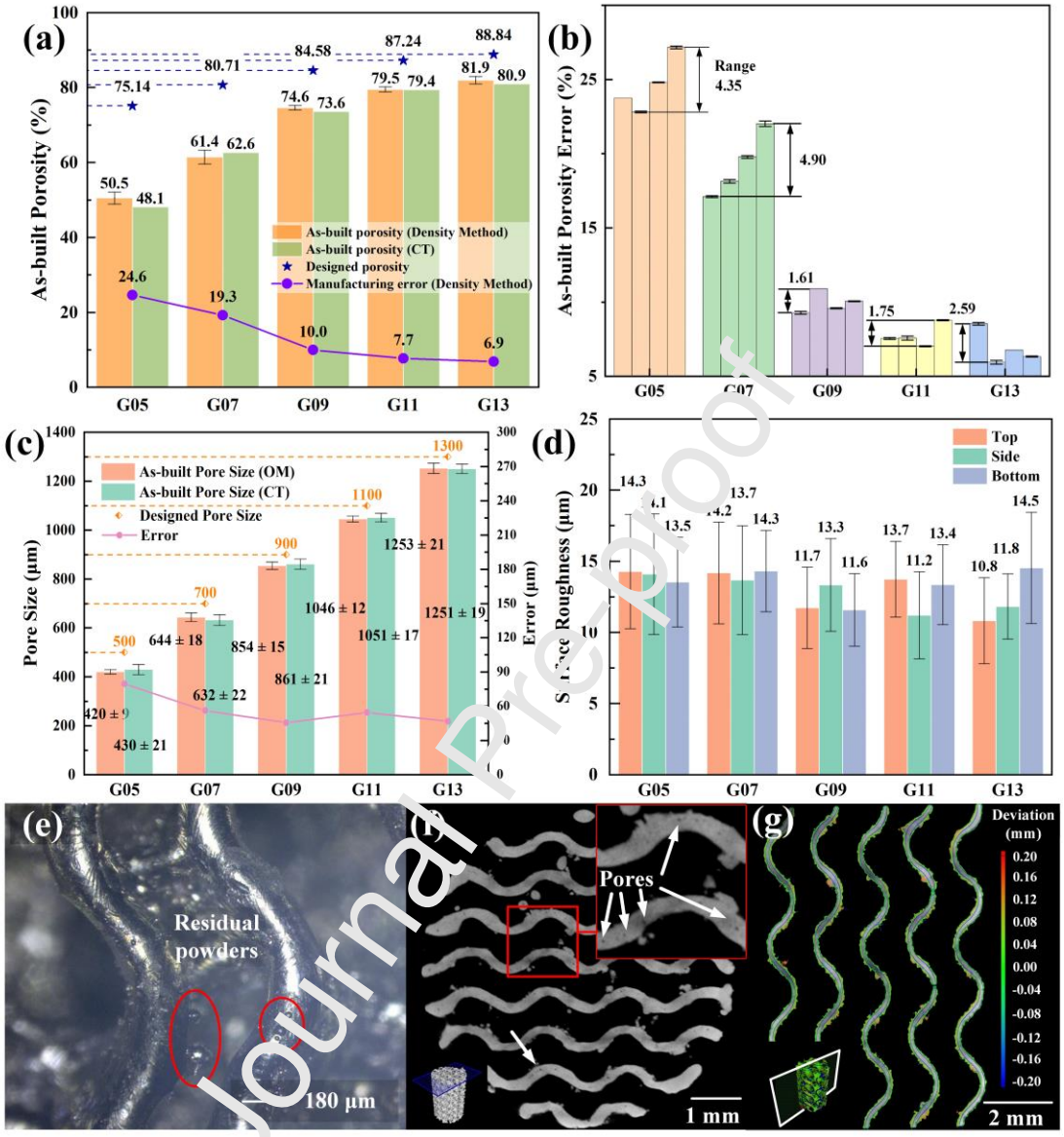

Fig. 3 (a) Measured and designed porosities of as-built samples. (b) Measured porosity values of four duplicate samples for each type of scaffold. (c) Measured and designed pore sizes of scaffolds and their errors (μm). (d) Surface roughness. (e) OM image of G05. (f) 2D CT image of G07. (g) CT and CAD data of G13.

The pore size was calculated by measuring the thickness values of each sample, as Fig. 3 (c) shows. The values of the as-built pore sizes were all less than the designed pore sizes. The manufactured external pore sizes ranged from 420–1,253 μm, and the internal pore sizes measured by the CT experiment were close to the external pore sizes. Compared to the designed pore sizes, the manufactured errors ranged from 46–

80 μm. No obvious relationship could be observed between the manufactured error and the designed porosity. The as-built pore sizes maintained remarkable stability when the designed thickness was equivalent. Table 4 shows the relative densities of the scaffolds, which ranged from 94.5–97.9%; the results show that the design porosities had little effect on RD.

Table 4 Relative densities of 316L stainless steel porous scaffolds

Scaffolds	G05	G07	G09	G11	G13
Relative Density (%)	94.8±0.4	96.0±0.3	97.9±0.8	94.5±0.6	95.8±0.8

As shown in Fig. 3 (d), the mean roughness of each sample at the top, side and bottom surfaces ranged from 10.8–14.5 μm. In the same sample, the roughness revealed few differences between the three surfaces. In general, the top surface was smoother than other two, but the mean roughness showed little difference between the five kinds of scaffolds. Fig. 3 (e) and (f) show the manufactured defects, such as residual powders and internal pores, and Fig. 3 (g) shows the deviations of the CAD and CT data of G13, which indicated that the manufactured thickness was larger than designed thickness.

3.2 Mechanical properties

Fig. 4 (a) shows the stress-strain curves of representative samples of all the test samples. G05–G13 represent five kinds of scaffolds with different designed porosities from 75.1–88.8%. The stress-strain curves were calculated by the force-displacement curve, which was directly measured by a compression test. Table 5 summarises the elastic modulus and yield strength values. G05 and G13 had the maximum and minimum elastic modulus and yield strength, respectively. G05 reached a 1116 ± 86 MPa elastic modulus value and a 29 ± 2 MPa yield strength.

Table 5 Mechanical properties of gyroid scaffolds

	Elastic modulus (MPa)					Yield strength (MPa)				
	1	2	3	Average	FEA	1	2	3	Average	FEA
G05	1113	1031	1203	1116±86	2004	31	27	28	29±2	43

G07	993	903	732	876±132	1661	21	19	17	19±2	31
G09	678	670	593	647±47	1362	11	10	11	11±0.6	24
G11	403	413	468	428±34	1158	9	8.7	8	8.6±0.6	19
G13	421	336	166	308±129	1026	6.6	7.9	6.3	6.9±0.8	15.9
P value			6.78×10^{-6}					1.97×10^{-8}		

To analyse the porosity trend of the elastic modulus and yield strength, Fig. 4 (b) shows the curves of the relationships between porosity and elastic modulus and yield strength, respectively, which both steadily decreased as porosity increased.

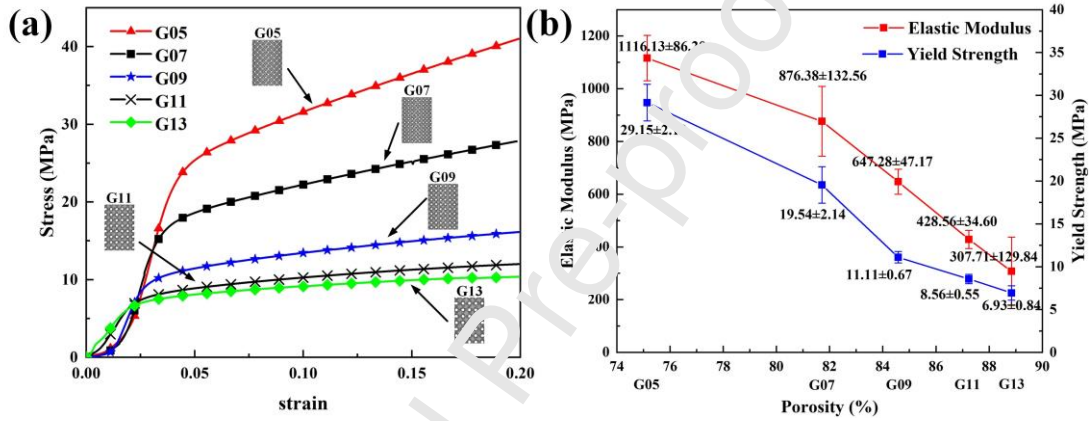

Fig. 4 (a) Nominal stress-strain curves of G05–G13 structures. (b) Drop curve between porosities and measured elastic modulus and yield strengths of as-built samples.

To compare the compression test and simulation, Fig. 5 (a)–(d) show the distributions at 1%, 20% and 32% strains. The stress concentration appears at the junctions of units and the middles of units, and the higher stress distribution (the red part in Fig. 5 (a)) is helical. At the 32% strain, the periphery of the cylindrical scaffold expanded, which was consistent with the experimental results. Fig. 5 (d) compares the G05 samples before and after the test; the strain was about 38%, and the scaffold showed superb toughness.

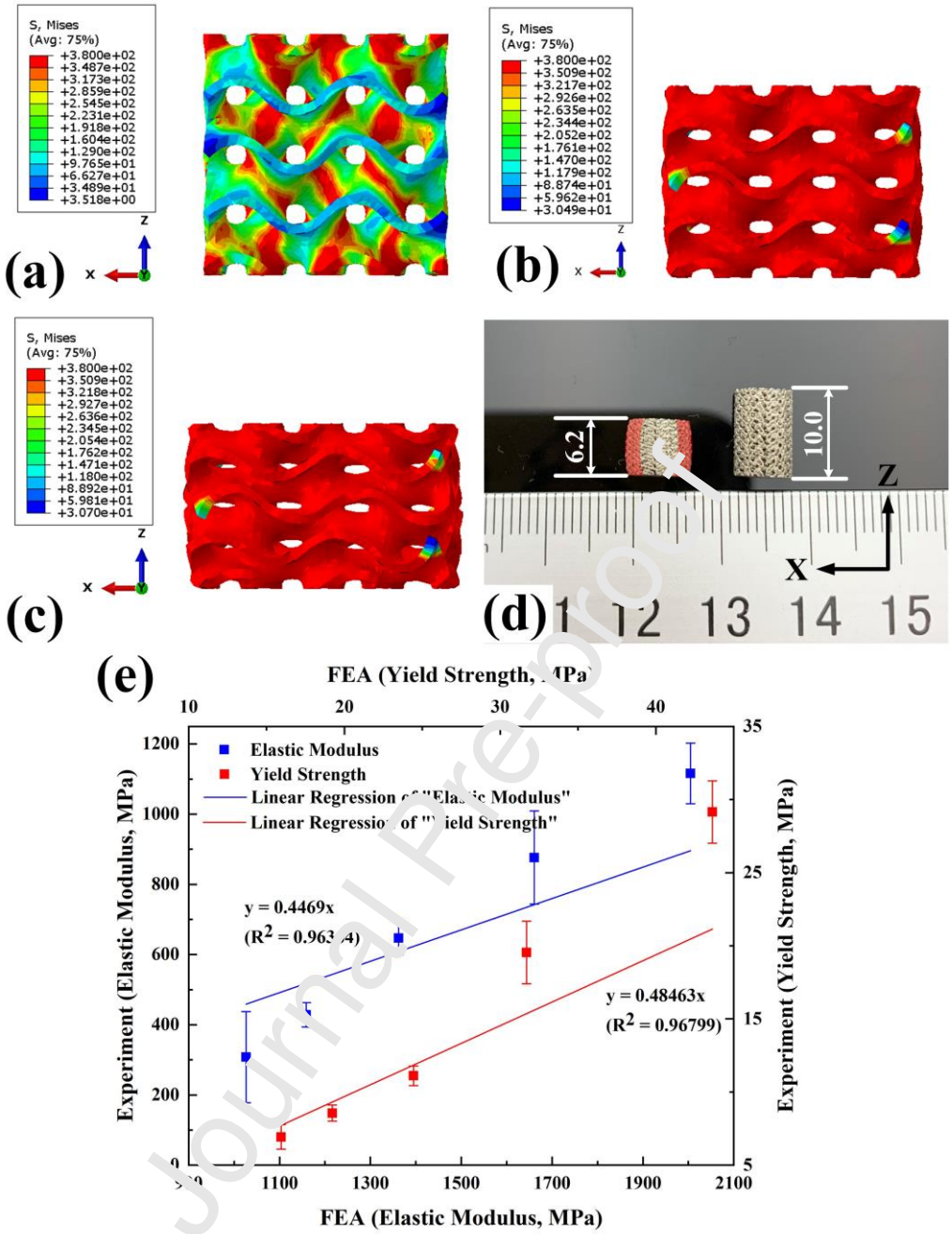

Fig. 5 The stress distribution and deformation of the simulation results of G05 at the strains of (a) 1%, (b) 20% and (c) 32%. (d) Comparison of tested and as-built samples of G05. (e) Correlation between the simulated and tested mechanical properties.

To evaluate the predictive capability, Fig. 5 (e) shows the relationship between the simulated and tested elastic modulus and yield strength; the blue and red lines represent the linear regressions with slopes of 0.45 and 0.48, respectively. The ratio of experimental to simulated results was also calculated from the coordinates; the elastic modulus ratio increased from 30% (G13, with 88.8% porosity) to 56% (G05, with

75.1% porosity), and the yield strength ratio increased from 43% (G13) to 67% (G05). The distribution of the lines and dots indicated that the predictive capability improved as the porosity declined.

3.3 Fluid flow analysis of scaffolds

For these five kinds of scaffolds, the value of the pressure drop between the inlet and outlet of the sample chamber was measured by a piezometric sensor at flow rates from 40–90 mL/min; Fig. 6 (a) shows the results. C05 (with 75.1% porosity) had the maximum pressure drop at the same flow rate, while C13 (with 88.8% porosity) had the minimum. Notably, in the linear regression lines in this figure, the pressure drop is approximately linear with the flow rates and matches the lines well, which agrees with the work of Montazerian et al. and Chor et al. [31, 59]. However, the pressure drop accelerated when the flow rate was greater than 80 mL/min, an effect of inertia [60, 61]. This also explained why permeability decreased as the flow rate increased in (Fig. 6 (b)), which shows the permeability of each scaffold at multiple flow rates. The permeability declined as the flow rate increased; the same phenomenon has also been observed by the others [60, 62, 63].

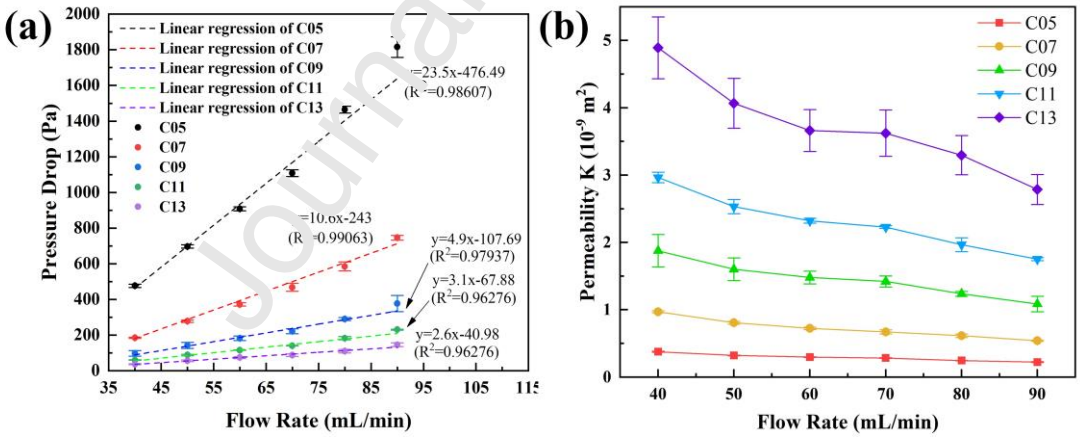

Fig. 6 (a) Measured pressure drops (ΔP) with different flow rates Q. (b) Calculated permeabilities K with different flow rates Q.

Fig. 7 (a)–(c) show the pressure and velocity distributions; Fig. 7 (b) shows that the fluid area closest to the walls had a lower velocity. The maximum velocity occurred in the central area. In the interior of the fluid, the same phenomenon was observed; Fig. 7 (c) shows two cross-section areas in vertical and horizontal directions. Predicting

the permeability while designing the scaffold can be helpful to optimise the design to balance mechanical properties and permeability; the latter would affect biological activities. Fig. 7 (d) shows the results of the simulations and experiments, the latter being less than the former. The predictive accuracy was evaluated by a linear regression line with a slope of 0.53, and the ratios of the tested and simulated results had greater with porosities (pore sizes). C05 and C13 had the lowest and highest ratio values, respectively: 46% and 73%. The experimental results ranged from 0.29 ± 0.05 × 10^{-9} m^2 to 3.91 ± 0.66 × 10^{-9} m^2.

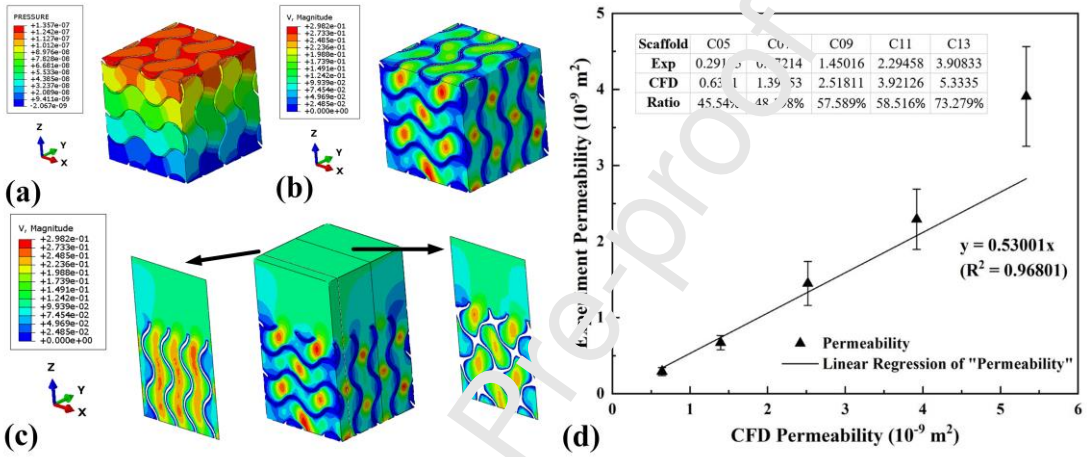

Fig. 7 The distribution of pressure and velocity of G11 (with 87.2% porosity and 1100 μm pore size): (a) pressure distribution, (b) velocity distribution and (c) vertical and horizontal velocity distribution within the sample. (d) Linear regression equation of the average permeability values of the CFD and experimental results.

3.4 Analysis of in vitro behaviour

Four duplicate samples were processed for each type of scaffold for in vitro study—two samples for cell culture and two for SEM observation. After 3 and 7 days of cell culture, the numbers of cells on the scaffolds and the control were calculated and normalised with the surface areas (see Table 1), as shown in Fig. 8 (g). Relative to the control, many fewer cells presented on the scaffolds on day 3. However, by day 7, the cell numbers on the control fell dramatically to fewer than half of those on day 3. However, the number of cells cultured on the scaffolds rose, except C09 (pore size = 900 μm, porosity = 84.6%). The number of cells on C13 rose by almost 237% by day 7. The cells on C11 and C07 showed a moderate increase to 86% and 60%,

respectively, followed by about a 33% increase on C05. The only exception to this cell-growth trend was C09. Although it seems more cells were present on C09 on day 3 than the rest of the scaffolds, on day 7, its cell number fell dramatically to fewer than half of those on day 3. Collectively, this indicated that all the scaffolds facilitated cell attachment after the initial culture stage. The scaffolds with large surface areas had much higher capacities to accommodate cell growth than the control, which was on a 2D surface of tissue culture–treated plastic. Still, the reason for sample C09's deviant behaviour and impeded cell proliferation in the subsequent stage remains unclear.

To observe the cells' morphological changes and proliferation from days 3–7, SEM experiments were performed. As shown in Fig. 8 (a), on day 3, most cells had a full, three-dimensional shape (the red circle), which means they started attaching to the surfaces of the scaffolds, and some extracellular matrices were observed (the yellow circle). Moreover, the cells had much flatter shapes on day 7 in Fig. 8 (b) (the red circle), and the arrow shows that many extracellular matrices were secreted. Fig. 8 (c) shows that after 3 days of culture, some cells had cellular pseudopods (the orange circle), which can anchor to surfaces tightly, spread out and connect to neighbouring cells. This indicated that cells were in good condition and tended to arrange in clusters. Then, interconnected cells (the orange circle) were observed on day 7, as shown in Fig. 8 (d). They connected, clung firmly to the surfaces and already arranged in clusters. In terms of cell proliferation, Fig. 8 (e) and (f) show more cells on the sample surface on day 7, which was consistent with the cell-growth data.

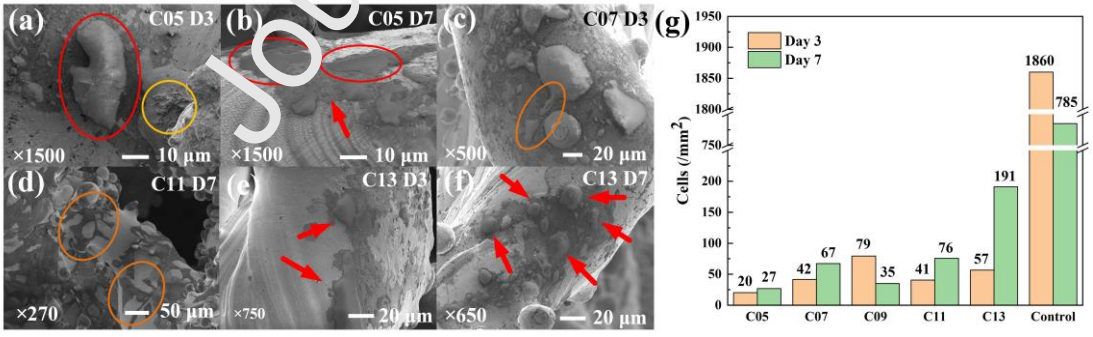

Fig. 8 SEM images of cell growth and morphology on days 3 and 7 (C05 = sample name, D3 = day 3). (a) Cells with 3D shapes and mineralised extracellular matrices. (b) Cells with flat shapes. (c) Cellular pseudopods. (d) Cell interconnections. (e,f) Cell proliferation. (g) Number of cells in samples and blank control at days 3 and 7.

4. Discussion

4.1 Morphology, accuracy of manufacturing and roughness of as-built samples

Both the top and side roughness were in the normal range of SLM-built parts without post-processing [64, 65].The variation of about 3.5 μm in the roughness values in different samples may have been caused by different heat fluxes, which are influenced by surface area and pore size and affect powder residue. As Fig. 3 (e) shows, residual powders were observed on the scaffold surfaces, which were caused by semi-melting. These residual powders may be the main reason for the rough surfaces [3, 36], so the bone scaffolds need surface post-processing to avoid adhered powders detaching during clinical application. The RD results indicated that the designed porosities had no influence on RD, and internal pores were observed in the scaffolds from the 2D CT images, which explained the low RD. Agreeing with [66], this suggests that designed porosities can be ignored when considering the RDs of scaffolds; optimising the processing parameters more effectively improves RD [8].

The pore sizes of as-built samples were significantly lower than the designed sizes, which was consistent with the results of other studies [41, 42, 67]. Arabnejad [42] controlled porosity by changing strut thickness while maintaining pore size; in that study, the porosity error increased with greater designed values (error from ~5–15%). In contrast, this study controlled porosity by changing the pore size and maintaining thickness, and the porosity error decreased with greater designed porosity (error from ~24.6–6.9%). The following may explain this difference. As with the manufactured error of pore size, the manufactured error of wall thickness was not affected by the designed porosity, the manufactured error ranged from 46–80 μm. As the designed porosity rose, the designed wall thickness remained 100 μm, while the designed pore size increased from 500 to 1300 μm. Therefore, for scaffolds with higher designed porosity, the manufactured error of thickness (pore size) had less effect on porosity error and fluctuated less. To minimise the porosity error, these two design methods should be combined while also necessarily considering the effect of size [36].

4.2 Mechanical properties

The mechanical property results revealed that the elastic modulus can be adjusted by

designing the scaffolds with varying porosity structures. Notably, nonlinear segments existed at the initial stage of each stress-strain curve in Fig. 4 (a). This could be explained by two reasons: 1) the top and bottom surfaces of the specimens were not perfectly horizontal, and they did not fully contact the upper and lower crossheads; 2) wire cutting deformed the bottom of the sample when removing parts from the platform, and this deformed region yields locally at the initial stage of compression, which agrees with the literature [68-70].

The prediction accuracy of the mechanical properties ranged from 30–56%, and the simulation results showed the same trend as the experiment results. The lack of accuracy in the simulation may be caused by the following reasons: 1) the CAD models used for simulation were considered perfect built samples, but the SLM-built samples had some manufacturing defects, such as surface roughness, internal pores and residual powders, which can affect mechanical behaviour; 2) the lower RD influenced the mechanical properties of the porous structures, so the processing parameters for the thin-walled parts need to be specially optimised, as Vilardell et al. suggested [71]; 3) although the as-built samples had greater thicknesses, they could not compensate for the lower scaffold mechanical strength caused by manufacturing defects; 4) the scaffolds with higher porosity had more defects due to longer overhang length [72], which weakened the scaffolds' mechanical properties and also explained why the experimental results matched the FEA results better as the porosity decreased.

As Table 6 shows, according to previous studies, the elastic moduli of the trabecular bone and porous scaffold ranged from 0.032–20.0 GPa and 0.57–28.59 GPa, respectively. In the current study, the 316L stainless steel gyroid scaffolds had suitable moduli at 0.31–1.12 GPa. Thanks to the large range of the moduli of trabecular bones, the gyroid structures can match their mechanical requirements by adjusting porosity. The yield strengths of porous scaffolds are generally designed to be greater than human bones to ensure that the scaffolds do not easily fail under load. Therefore, the gyroid scaffolds fabricated by 316L stainless steel met the mechanical requirements and are promising for future application.

Table 6 Comparison of the elastic moduli (GPa) and yield strengths (MPa) of trabecular bones and porous scaffolds measured by experiments or simulations.

	Elastic modulus (GPa)	Yield strength (MPa)

Arun et al. [48]	0.91–10.42[bs]	24.4–152.3[bs]
Ola et al. [50]	-	0.9–94.9[be]
Kevin et al. [51]	~1.1–28.6[be]	~9.3–327.5[be]
Jayanthi et al. [73]	~0.57–2.92[be]	~7.3–163.0[be]
Keaveny et al. [74]	0.032-0.355[ae]	-
David et al. [75]	0.090–0.536[ae]	0.56–3.71[ae]
Rho et al. [76]	0.76–20[ae]	-
Current study (average)	~ 0.31–1.12[be]	~ 6.9–29.2[be]

[a] Trabecular bone, [b] porous scaffold

[e] Experiment, [s] simulation

4.3 Mass-transport behaviour of scaffolds

Permeability, as measured by experiments, reached 46–73% of the CFD results, and the simulation showed a similar trend as the experiments: permeability increasing as porosity and pore size increased. The same phenomenon was observed by du Plessis et al. [34], whose ratio of experimental results to CFD results was about 60–70% of the simulation results; it was about 29–43% in Truscello et al. [77].

The difference between the experimental and simulated permeabilities was likely caused by the following: 1) the pore sizes of as-built samples were smaller than those of the CAD models, thus reducing permeability; 2) for the experiment, the pressure drop from the pressure-monitoring point to the inlet and outlet surfaces of the sample cannot be ignored, as they cause ΔP to be greater than the real value and shrink the calculated permeability value; 3) the surfaces of the CAD models were considered smooth surfaces, while the samples' surfaces were rough with residual powders, which slows the flow of fluid close to the scaffolds' surfaces. G13 was less affected by this factor due to its large pore size, so its experimental permeability reached 73% of the CFD result. Thus, the influence of rough surfaces on the permeability of a sample with a small pore size is more significant, which is consistent with the work of Davar Ali et al. [78].

A higher fluid velocity in the middle of the scaffold channel was observed in the velocity distribution of the CFD results, which encourages cells to migrate toward the centre of the scaffold. The area close to the scaffold had lower fluid velocity, which

was caused by the obstacle of the scaffold. This phenomenon was more significant for the as-built samples due to their rougher surfaces.

Scaffold permeability should be designed as closely as possible to the permeability range of human bones, the values of which Table 7 shows. Gyroid structures can meet the transmission requirements of human bones, and it seemed that greater permeability could be achieved by designing larger pore sizes and porosities. Such adjustable, predictable permeability allows customising the design to meet the mass-transfer requirements of different types of bones.

Table 7 Comparing the permeability of trabecular bones and porous scaffolds

	Arjunan et al. [48]	Montazerian et al. [31]	Chor et al. [59]	Dabrowski et al. [79]	Truscello et al. [77]	Beaudoin et al. [80]	Nauman et al. [81]	Current study (average)
K (10^{-9} m^2)	68.1-180.0[bs]	1.65–4.02[be]	0.183-0.247[be]	0.0153-1.37[be]	0.052-3.61[bs]	0.467-14.8[as]	0.0268-20.0[ae]	~0.29-3.91[be]

[a] Trabecular bone, [b] porous scaffold

[e] Experiment, [s] simulation

4.4 Cell behaviour

Based on the results in Fig. 8 (g), moderate cell growth occurred on the 75.1% and 81.7% porosity scaffolds on day 3. The number of cells on the 81.7% porosity scaffold was larger than the 75.1% porosity scaffold. Because the former had better permeability, it exhibited a better growth rate on day 7. Notably, the chief limitation on cell proliferation on the 75.1% and 81.7% porosity scaffolds was permeability despite their large surface areas. The 87.2% and 88.8% porosity scaffolds both had better permeabilities than the others. Although their cell-attachment values at the initial culture stage were not the highest due to their small surface areas, they both witnessed high rates of cell growth. Although the 88.8% porosity scaffold had only a few cells on day 3, it had both the largest growth rate and number of cells on day 7.

The same results were observed by Van [82]: scaffolds with higher permeabilities stimulate cell proliferation due to their better abilities to supply oxygen and nutrients. Their geometric features also supported cell proliferation: gyroid structures have zero mean curvature, and their Gaussian curvature is less than or equal to zero everywhere, the same characteristics as human bones [83]. However, this must be confirmed by future studies. The capillary effect also likely affected the rate of cell immigration since capillary action was affected by pore size and porosity [84]. The 88.8% porosity scaffold had the highest rate of cell growth, which is consistent with Daniel et al.'s finding that the scaffold with the largest pore size had the highest rising rate of fluid, entailing that a larger pore size can raise the rate of cell immigration [85].

Although the cell-growth rate appeared to rise with greater porosity and pore sizes, the 84.6% porosity scaffold experienced the opposite. Its number of cells was the largest at the initial stage, but it decreased in the subsequent culture time. Perhaps at the initial stage of cell attachment, the permeability and pore size affected the rate of cell seeding. The scaffolds with lower permeabilities had more cells seeding on the scaffolds due to low fluid velocities, but cells are difficult to seed on scaffolds with low designed porosities due to small pore size [82]. Because the 84.6% scaffold had a good balance of permeability and pore size, it had the highest rate of adhesion to the scaffold on day 3; with continuous culture, however, the growth rate possibly slowed due to the scaffold's limited permeability when too many cells presented on the surface. This phenomenon requires confirmation by further studies using different seeding densities.

In general, permeability is the principal factor of the cell-proliferation rate. Surface area and permeability determine the upper limit of the number of cells on scaffolds. Except for the cells on the 84.6% porosity scaffold, which decreased due to its transport performance because it could not meet the needs of all the cells that attached to its surface at an early stage, the cells all increased at different rates. In the 7 days of cell culture, no scaffold reached the upper limit of the cells that could be accommodated by its available surface area. In future studies, it would be interesting to resolve whether a 75.1% porosity scaffold (with a larger surface area and lower permeability) or an 88.8% porosity scaffold (with a smaller surface area and higher permeability) can support more cells and cell growth with cultures of more than 7 days. In the present study, the more permeable scaffolds had better bone-cell recovery

because of their high rates of cell growth. However, when executing a design, mechanical properties should also be considered to meet mechanical performance requirements.

5. Conclusions

In this study, five gyroid scaffold designs were fabricated to investigate their manufacturability. The influence of the design parameters on the mechanical and transport properties of the scaffolds was investigated via simulations, which were followed by experiments that evaluated the simulations' predictive power. The biocompatibility of the gyroid scaffolds and the influences of certain parameters on cell growth were evaluated. The results include the following:

1) The 316L stainless steel gyroid structures processed by SLM presented stable manufacturability, which was proven by the accuracy of the porosity and the manufacturing error of the thickness. Moreover, it was found that the design method used in this study can reduce the manufacturing porosity error in high-porosity scaffolds.
2) The 316L stainless steel gyroid scaffolds fabricated by SLM were found to have adjustable mechanical properties; this trend was predicted via FEA, although some differences existed. The elastic moduli and yield strengths of the gyroid scaffolds ranged from 0.31–1.12 GPa and 6.93–29.15 MPa, respectively. Their mechanical properties decreased as porosity increased, which satisfies the requirements of human trabecular bones. The ratio of experimental and simulated results ranged from 30–56%, a difference mainly caused by manufacturing defects, such as low RD. Processing parameters optimised for porous parts should be studied in future work to reduce the difference between experimental and simulated results.
3) The mass-transport behaviour of the gyroid scaffolds was studied through both experimental and simulated methods. Their permeabilities ranged from 0.29×10^{-9} to 3.91×10^{-9} m^2, which was suitable for the wide range of human trabecular bones, and their permeabilities increased as pore size and porosity increased. Their complex structures also reduced the flow rate of liquid near the walls of the scaffolds, which helped cells attach to their surfaces. The CFD simulation predicted the scaffolds' permeabilities, with the highest accuracy reaching 73%. The roughness of the scaffolds' surfaces can

influence transmission performance, especially for scaffolds with small pore sizes.

4) The cells' behaviour was investigated through 3- and 7-day cell-culture experiments. They all showed biocompatibility; the number of cells rose, and cell attachment to the surfaces of the scaffolds was observed 7 days after the culture was taken. The largest number of cells was measured on the 84.6% porosity scaffold on day 3; however, the 88.8% porosity scaffold had the most cells on day 7. Surface area and permeability can both affect the degrees of cell adhesion and proliferation, although permeability plays the main role in cell proliferation in the initial stage.
5) After comprehensively considering the characteristics of the gyroid scaffold, it was determined that the best design method includes satisfying mechanical property requirements and having larger porosity (pore size) to obtain higher permeability and thus promote bone repair.

In summary, 316L stainless steel gyroid scaffolds manufactured by SLM were found suitable for use in bone scaffolds. This research reveals the influence of porous structure parameters on the manufacturability and mechanical, transmission and biocompatibility requirements of bone scaffolds. Its results are significant for guiding the choice of suitable parameters, it verifies the predictability of mechanical and transport properties, and it summarises the possible influences on simulation accuracy, which can provide future research directions. This study also reveals that permeability plays the main role in the rate of cell growth in the initial stage, which is important for the design of efficient bone-repair scaffolds. In future research, it would be interesting to judge the bone-repair effects of scaffolds with a cell-culture experiment for more than 7 days in an *in vivo* experiment.

Acknowledgements

This paper was supported by the National Natural Science Foundation of China (Grant No: 51975073, No. 51805052), the Fundamental Research Funds for the Central Universities (No. 2018CDXYJX0019), Chongqing Science and Technology Bureau (No. cstc2018 jszx-cyzdX0102) and the China Scholarship Council (CSC). The authors would like to thank David Thompson (Loughborough University) for the SLM manufacturing assistance, Dr Ran Tao (The Hong Kong University of Science

and Technology) for the fluid mechanics theory assistance, Andrew Wald (Loughborough University) for the powder size distribution experiment, Pinghua Liang and Xiaojie Fan (Chongqing University) for the permeability test experiment.

References

[1] Onal E, Frith JE, Jurg M, Wu X, Molotnikov A. Mechanical Properties and In Vitro Behavior of Additively Manufactured and Functionally Graded Ti6Al4V Porous Scaffolds. METALS-BASEL 2018;8:200.

[2] Eshraghi S, Das S. Micromechanical finite-element modeling and experimental characterization of the compressive mechanical properties of polycaprolactone–hydroxyapatite composite scaffolds prepared by selective laser sintering for bone tissue engineering. ACTA BIOMATER 2012;8:3138.

[3] Čapek J, Machová M, Fousová M, Kubásek J, Vojtěch D, Fojt J, Jablonská E, Lipov J, Ruml T. Highly porous, low elastic modulus 316L stainless steel scaffold prepared by selective laser melting. Materials Science and Engineering: C 2016;69:631.

[4] Hallab NJ, Bundy KJ, O'Connor K, Moses RL, Jacobs JJ. Evaluation of metallic and polymeric biomaterial surface energy and surface roughness characteristics for directed cell adhesion. TISSUE ENG 2001;7:55.

[5] Sing SL. Concepts of Selective Laser Melting for Orthopaedic Implants. Selective Laser Melting of Novel Titanium-Tantalum Alloy as Orthopaedic Biomaterial. Singapore: Springer Singapore, 2019. p.9.

[6] Markhoff J, Wieding J, Weissmann V, Pasold J, Jonitz-Heincke A, Bader R. Influence of Different Three-Dimensional Open Porous Titanium Scaffold Designs on Human Osteoblasts Behavior in Static and Dynamic Cell Investigations. MATERIALS 2015;8:5490.

[7] Han Q, Gu Y, Setchi R, Lacan F, Johnston R, Evans SL, Yang S. Additive manufacturing of high-strength crack-free Ni-based Hastelloy X superalloy. Additive Manufacturing 2019;30:100919.

[8] Song J, Tang Q, Feng Q, Ma S, Setchi R, Liu Y, Han Q, Fan X, Zhang M. Effect of heat treatment on microstructure and mechanical behaviours of 18Ni-300 maraging steel manufactured by selective laser melting. Optics & Laser Technology 2019;120:105725.

[9] Ma C, Gu D, Dai D, Zhang H, Zhang H, Yang J, Guo M, Du Y, Gao J. Microstructure evolution and high-temperature oxidation behaviour of selective laser melted TiC/TiAl composites. Surface and Coatings Technology 2019;375:534.

[10] Carluccio D, Xu C, Venezuela J, Cao Y, Kent D, Bermingham M, Demir AG, Previtali B, Ye Q, Dargusch M. Additively manufactured iron-manganese for biodegradable porous load-bearing bone scaffold applications. ACTA BIOMATER 2020;103:346.

[11] Li Y, Pavanram P, Zhou J, Lietaert K, Taheri P, Li W, San H, Leeflang MA, Mol JMC, Jahr H, Zadpoor AA. Additively manufactured biodegradable porous zinc. ACTA BIOMATER 2020;101:609.

[12] du Plessis A, Broeckhoven C, Yadroitsava I, Yadroitsev I, Hands CH, Kunju R, Bhate D. Beautiful and Functional: A Review of Biomimetic Design in Additive Manufacturing. Additive Manufacturing 2019;27:408.

[13] Yuan L, Ding S, Wen C. Additive manufacturing technology for porous metal implant applications and triple minimal surface structures: A review. Bioactive Materials 2019;4:56.

[14] Maconachie T, Leary M, Lozanovski B, Zhang X, Qian M, Faruque O, Brandt M. SLM lattice structures: Properties, performance, applications and challenges. MATER DESIGN 2019;183:108137.

[15] Brentel AS, de Vasconcellos LM, Oliveira MV, Graca ML, de Vasconcellos LG, Cairo CA, Carvalho YR. Histomorphometric analysis of pure titanium implants with porous surface versus rough surface. J APPL ORAL SCI 2006;14:213.

[16] Oliveira MV, Pereira LC, Cairo CAA. Porous Structure Characterization in Titanium Coating for Surgical Implants. Materials Research 2002;5:269.

[17] Barba D, Alabort E, Reed RC. Synthetic bone: Design by additive manufacturing. ACTA BIOMATER 2019;97:637.

[18] Van Bael S, Chai YC, Truscello S, Moesen M, Kerckhofs G, Van Oosterwyck H, Kruth JP, Schrooten J. The effect of pore geometry on the in vitro biological behavior of human periosteum-derived cells seeded on selective laser-melted Ti6Al4V bone scaffolds. ACTA BIOMATER 2012;8:2824.

[19] Hutmacher DW, Schantz JT, Lam CXF, Tan KC, Lim TC. State of the art and future directions of scaffold-based bone engineering from a biomaterials perspective. J TISSUE ENG REGEN M 2007;1:245.

[20] Hollister SJ. Scaffold Design and Manufacturing: From Concept to Clinic. ADV MATER 2009;21:3330.

[21] Van Bael S, Kerckhofs G, Moesen M, Pyka G, Schrooten J, Kruth JP. Micro-CT-based improvement of geometrical and mechanical controllability of selective laser melted Ti6Al4V porous structures. MAT SCI ENG A-STRUCT 2011;528:7423.

[22] Yang L, Ferrucci M, Mertens R, Dewulf W, Yan C, Shi Y, Yang S. An investigation into the effect of gradients on the manufacturing fidelity of triply periodic minimal surface structures with graded density fabricated by selective laser melting. J MATER PROCESS TECH 2020;275:116367.

[23] Yu T, Hyer H, Sohn Y, Bai Y, Wu D. Structure-property relationship in high strength and lightweight AlSi10Mg microlattices fabricated by selective laser melting. MATER DESIGN 2019;182:108062.

[24] Ma S, Tang Q, Feng Q, Song J, Han X, Guo F. Mechanical behaviours and mass transport properties of bone-mimicking scaffolds consisted of gyroid structures manufactured using selective laser melting. J MECH BEHAV BIOMED 2019;93:158.

[25] Oliveira JP, Santos TG, Miranda RM. Revisiting fundamental welding concepts to improve additive manufacturing: From theory to practice. PROG MATER SCI 2020;107:100590.

[26] Oliveira JP, LaLonde AD, Ma J. Processing parameters in laser powder bed fusion metal additive manufacturing. MATER DESIGN 2020;193:108762.

[27] Abueidda DW, Elhebeary M, Shiang CA, Pang S, Abu Al-Rub RK, Jasiuk IM. Mechanical properties of 3D printed polymeric Gyroid cellular structures: Experimental and finite element study. MATER DESIGN 2019;165:107597.

[28] Guo X, Zheng X, Yang Y, Yang X, Yi Y. Mechanical behavior of TPMS-based scaffolds: a comparison between minimal surfaces and their lattice structures. SN Applied Sciences 2019;1:1145.

[29] Garner E, Kolken HMA, Wang CCL, Zadpoor AA, Wu J. Compatibility in microstructural optimization for additive manufacturing. Additive Manufacturing 2019;26:65.

[30] Maskery I, Aremu AO, Parry L, Wildman RD, Tuck CJ, Ashcroft IA. Effective design and

simulation of surface-based lattice structures featuring volume fraction and cell type grading. MATER DESIGN 2018;155:220.

[31] Montazerian H, Mohamed MGA, Montazeri MM, Kheiri S, Milani AS, Kim K, Hoorfar M. Permeability and mechanical properties of gradient porous PDMS scaffolds fabricated by 3D-printed sacrificial templates designed with minimal surfaces. ACTA BIOMATER 2019;96:149.

[32] Yan C, Hao L, Hussein A, Young P, Raymont D. Advanced lightweight 316L stainless steel cellular lattice structures fabricated via selective laser melting. MATER DESIGN 2014;55:533.

[33] Yánez A, Cuadrado A, Martel O, Afonso H, Monopoli D. Gyroid porous titanium structures: A versatile solution to be used as scaffolds in bone defect reconstruction. MATER DESIGN 2018;140:21.

[34] du Plessis A, Yadroitsava I, Yadroitsev I, le Roux SG, Blaine DC. Numerical comparison of lattice unit cell designs for medical implants by additive manufacturing. Virtual and Physical Prototyping 2018;13:266.

[35] Boniotti L, Foletti S, Beretta S, Patriarca L. Analysis of strain and stress concentrations in micro-lattice structures manufactured by SLM. RAPID PROTOTYPING J 2019;26:370.

[36] Ataee A, Li Y, Brandt M, Wen C. Ultrahigh-strength titanium gyroid scaffolds manufactured by selective laser melting (SLM) for bone implant applications. ACTA MATER 2018;158:354.

[37] Lyczkowska-Widlak E, Lochynski P, Nawrat G, Chlebus E. Comparison of electropolished 316L steel samples manufactured by SLM and traditional technology. RAPID PROTOTYPING J 2019;25:566.

[38] Faia-Torres AB, Guimond-Lischer S, Rottmar M, Charnley M, Goren T, Maniura-Weber K, Spencer ND, Reis RL, Textor M, Neves NM. Differential regulation of osteogenic differentiation of stem cells on surface roughness gradients. BIOMATERIALS 2014;35:9023.

[39] Albrektsson T, Wennerberg A. Oral implant surfaces: Part 1--review focusing on topographic and chemical properties of different surfaces and in vivo responses to them. The International journal of prosthodontics 2004;17:536.

[40] Trelewicz JR, Halada GP, Donaldson OK, Manogharan G. Microstructure and Corrosion Resistance of Laser Additively Manufactured 316L Stainless Steel. JOM-US 2016;68:850.

[41] Choy SY, Sun C, Leong KF, Wei J. Compressive properties of Ti-6Al-4V lattice structures fabricated by selective laser melting: Design, orientation and density. Additive Manufacturing 2017;16:213.

[42] Arabnejad S, Burnett Johnston R, Pura JA, Singh B, Tanzer M, Pasini D. High-strength porous biomaterials for bone replacement: A strategy to assess the interplay between cell morphology, mechanical properties, bone ingrowth and manufacturing constraints. ACTA BIOMATER 2016;30:345.

[43] Liverani E, Toschi S, Ceschini L, Fortunato A. Effect of selective laser melting (SLM) process parameters on microstructure and mechanical properties of 316L austenitic stainless steel. J MATER PROCESS TECH 2017;249:255.

[44] Montero-Sistiaga ML, Godino-Martinez M, Boschmans K, Kruth J, Van Humbeeck J, Vanmeensel K. Microstructure evolution of 316L produced by HP-SLM (high power selective laser melting). Additive Manufacturing 2018;23:402.

[45] Laleh M, Hughes AE, Xu W, Gibson I, Tan MY. Unexpected erosion-corrosion behaviour of 316L stainless steel produced by selective laser melting. CORROS SCI 2019;155:67.

[46] Alsalla H, Hao L, Smith C. Fracture toughness and tensile strength of 316L stainless steel cellular lattice structures manufactured using the selective laser melting technique. Materials Science and Engineering: A 2016;669:1.

[47] Lei H, Li C, Meng J, Zhou H, Liu Y, Zhang X, Wang P, Fang D. Evaluation of compressive properties of SLM-fabricated multi-layer lattice structures by experimental test and μ-CT-based finite element analysis. MATER DESIGN 2019;169:107685.

[48] Arjunan A, Demetriou M, Baroutaji A, Wang C. Mechanical performance of highly permeable laser melted Ti6Al4V bone scaffolds. J MECH BEHAV BIOMED 2019:103517.

[49] Feng Q, Tang Q, Liu Y, Setchi R, Soe S, Ma S, Bai L. Quasi-static analysis of mechanical properties of Ti6Al4V lattice structures manufactured using selective laser melting. The International Journal of Advanced Manufacturing Technology 2018;94:2301.

[50] Harrysson OLA, Cansizoglu O, Marcellin-Little DJ, Cormier DR, West HA. Direct metal fabrication of titanium implants with tailored materials and mechanical properties using electron beam melting technology. Materials Science and Engineering: C 2008;28:366.

[51] Hazlehurst K, Wang CJ, Stanford M. Evaluation of the stiffness characteristics of square pore CoCrMo cellular structures manufactured using laser melting technology for potential orthopaedic applications. MATER DESIGN 2013;51:949.

[52] Lozanovski B, Leary M, Tran P, Shidid D, Qian M, Choong P, Brandt M. Computational modelling of strut defects in SLM manufactured lattice structures. MATER DESIGN 2019;171:107671.

[53] Zhang X, Fang G, Xing L, Liu W, Zhou J. Effect of porosity variation strategy on the performance of functionally graded Ti-6Al-4V scaffolds for bone tissue engineering. MATER DESIGN 2018;157:523.

[54] Tao R, Ng T, Su Y, Li Z. A microfluidic rectifier for Newtonian fluids using asymmetric converging–diverging microchannels. PHYS FLUIDS 2020;32:52010.

[55] Ali D, Sen S. Finite element analysis of mechanical behavior, permeability and fluid induced wall shear stress of high porosity scaffolds with gyroid and lattice-based architectures. J MECH BEHAV BIOMED 2017;75:262.

[56] Scherer MRJ. Double-Gyoid-Structured Functional Materials: Synthesis and Applications. Cham: Springer International Publishing, 2013. p.211.

[57] Truscello S, Kerckhofs G, Van Bael S, Pyka G, Schrooten J, Van Oosterwyck H. Prediction of permeability of regular scaffolds for skeletal tissue engineering: A combined computational and experimental study. ACTA BIOMATER 2012;8:1648.

[58] W. Sobieski AT. Darcy's and Forchheimer's laws in practice. Part 1. The experiment. Tech. Sci. 2011:290.

[59] Chor MV, Li W. A permeability measurement system for tissue engineering scaffolds. MEAS SCI TECHNOL 2007;18:208.

[60] Bobbert FSL, Lietaert K, Eftekhari AA, Pouran B, Ahmadi SM, Weinans H, Zadpoor AA. Additively manufactured metallic porous biomaterials based on minimal surfaces: A unique combination of topological, mechanical, and mass transport properties. ACTA BIOMATER 2017;53:572.

[61] Tao R, Jin Y, Gao X, Li Z. Flow characterization in converging-diverging microchannels. PHYS

FLUIDS 2018;30:112004.

[62] Castro APG, Pires T, Santos JE, Gouveia BP, Fernandes PR. Permeability versus Design in TPMS Scaffolds. Materials (Basel, Switzerland) 2019;12:1313.

[63] Rahbari A, Montazerian H, Davoodi E, Homayoonfar S. Predicting permeability of regular tissue engineering scaffolds: scaling analysis of pore architecture, scaffold length, and fluid flow rate effects. COMPUT METHOD BIOMEC 2017;20:231.

[64] Delgado J, Ciurana J, Rodríguez CA. Influence of process parameters on part quality and mechanical properties for DMLS and SLM with iron-based materials. The International Journal of Advanced Manufacturing Technology 2012;60:601.

[65] Kerckhofs G, Pyka G, Van Bael S, Schrooten J, Wevers M. Investigation of the influence of surface roughness modification of bone tissue engineering scaffolds. SkyScan User Meeting 2010, Date: 2010/07/07-2010/07/09, Location: Mechelen, Belgium: SkyScan User Meeting 2010 Abstract Book, 2010.

[66] Echeta I, Feng X, Dutton B, Leach R, Piano S. Review of defects in lattice structures manufactured by powder bed fusion. The International Journal of Advanced Manufacturing Technology 2020;106:2649.

[67] Melchels FPW, Bertoldi K, Gabbrielli R, Velders AH, Feijen J, Grijpma DW. Mathematically defined tissue engineering scaffold architectures prepared by stereolithography. BIOMATERIALS 2010;31:6909.

[68] Yan C, Hao L, Hussein A, Raymont D. Evaluations of cellular lattice structures manufactured using selective laser melting. INT J MACH TOOL MANU 2012;62:32.

[69] McKown S, Shen Y, Brookes WK, Sutcliffe CJ, Cantwell WJ, Langdon GS, Nurick GN, Theobald MD. The quasi-static and blast loading response of lattice structures. INT J IMPACT ENG 2008;35:795.

[70] Feng Q, Tang Q, Soe S, Liu Y, Setchi R. An Investigation into the Quasi-Static Response of Ti6Al4V Lattice Structures Manufactured Using Selective Laser Melting. In: Setchi R, Howlett RJ, Liu Y, Theobald P, ^editors. Cham. Springer International Publishing, 2016. p.399.

[71] Vilardell AM, Takezawa A, du Plessis A, Takata N, Krakhmalev P, Kobashi M, Yadroitsava I, Yadroitsev I. Topology optimization and characterization of Ti6Al4V ELI cellular lattice structures by laser powder bed fusion for biomedical applications. Materials Science and Engineering: A 2019;766:138330.

[72] Xu Y, Zhang D, Zhou Y, Wang W, Cao X. Study on topology optimization design, manufacturability, and performance evaluation of Ti-6Al-4V porous structures fabricated by selective laser melting (SLM). MATERIALS 2017;10:1048.

[73] Parthasarathy J, Starly B, Raman S. A design for the additive manufacture of functionally graded porous structures with tailored mechanical properties for biomedical applications. J MANUF PROCESS 2011;13:160.

[74] Keaveny TM, Pinilla TP, Crawford RP, Kopperdahl DL, Lou A. Systematic and random errors in compression testing of trabecular bone. J ORTHOP RES 1997;15:101.

[75] Kopperdahl DL, Keaveny TM. Yield strain behavior of trabecular bone. J BIOMECH 1998;31:601.

[76] Rho JY, Ashman RB, Turner CH. Young's modulus of trabecular and cortical bone material:

ultrasonic and microtensile measurements. J BIOMECH 1993;26:111.

[77] Truscello S, Kerckhofs G, Van Bael S, Pyka G, Schrooten J, Van Oosterwyck H. Prediction of permeability of regular scaffolds for skeletal tissue engineering: A combined computational and experimental study. ACTA BIOMATER 2012;8:1648.

[78] Ali D, Sen S. Computational Fluid Dynamics Study of the Effects of Surface Roughness on Permeability and Fluid Flow-Induced Wall Shear Stress in Scaffolds. ANN BIOMED ENG 2018;46:2023.

[79] Dabrowski B, Swieszkowski W, Godlinski D, Kurzydlowski KJ. Highly porous titanium scaffolds for orthopaedic applications. J Biomed Mater Res B Appl Biomater 2010;95:53.

[80] Beaudoin AJ, Mihalko WM, Krause WR. Finite element modelling of polymethylmethacrylate flow through cancellous bone. J BIOMECH 1991;24:127.

[81] Nauman EA, Fong KE, Keaveny TM. Dependence of Intertrabecular Permeability on Flow Direction and Anatomic Site. ANN BIOMED ENG 1999;27:517.

[82] Van Bael S, Chai YC, Truscello S, Moesen M, Kerckhofs G, Van Oosterwyck H, Kruth IP, Schrooten J. The effect of pore geometry on the in vitro biological behavior of human periosteum-derived cells seeded on selective laser-melted Ti6Al4V bone scaffolds. ACTA BIOMATER 2012;8:2824.

[83] Callens SJP, Uyttendaele RJC, Fratila-Apachitei LE, Zadpoor AA. Substrate curvature as a cue to guide spatiotemporal cell and tissue organization. BIOMATERIALS 2020;232:119739.

[84] Bai H, Wang D, Delattre B, Gao W, De Coninck J, Li S, Tomsia AP. Biomimetic gradient scaffold from ice-templating for self-seeding of cells with capillary effect. ACTA BIOMATER 2015;20:113.

[85] Oh DS, Kim YJ, Hong M, Han M, Kim K. Effect of capillary action on bone regeneration in micro-channeled ceramic scaffolds. CERAM INT 2014;40:9583.

Declaration of interests

☒ The authors declare that they have no known competing financial interests or personal relationships that could have appeared to influence the work reported in this paper.

☐The authors declare the following financial interests/personal relationships which may be considered as potential competing interests:

Shuai Ma: Methodology, Data curation, Investigation, Writing - original draft. **Qian Tang**: Resources, Supervision, Project administration. **Xiaoxiao Han**: Supervision, Writing - review & editing. **Qixiang Feng**: Methodology, Investigation. **Jun Song**: Investigation. **Rossitza Setchi**: Writing - review & editing. **Ying Liu**: Writing - review & editing. **Yang Liu**: Writing - review & editing. **Athanasios Goulas**: Writing - review & editing. **Daniel S.Engstrøm**: Writing - review & editing. **Yau Yau Tse**: Investigation. **Ni Zhen**: Investigation.

Highlights:

- Proposing a design method to improve the accuracy of manufactured porosity of high-porosity scaffolds.
- Comprehensively studying the manufacturability, mechanical and mass transport properties, and biocompatibility of gyroid scaffolds.
- The simulation of the mechanical and mass-transport properties of scaffolds both showed predictability.
- Greater pore size gave bone scaffolds higher permeability, which promotes bone repair
- The factors possibly affecting the prediction accuracy of the mechanical and mass-transport properties of lattice scaffolds were summarised.

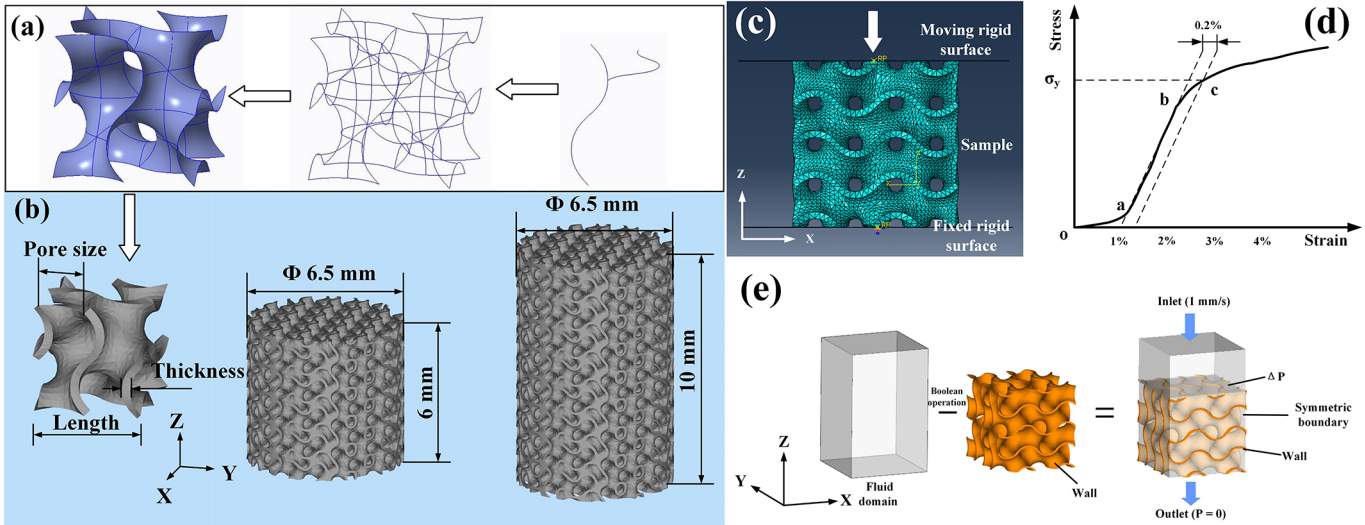
(a)
(b)
Pore size
Thickness
Length
Z
Y
X
Φ 6.5 mm
6 mm
Φ 6.5 mm
10 mm
(c)
Moving rigid surface
Sample
Fixed rigid surface
Z
X
(d)
Stress
0.2%
σy
a
b
c
0
1%
2%
3%
4%
Strain
(e)
Inlet (1 mm/s)
Boolean operation
=
ΔP
Symmetric boundary
Wall
Fluid domain
Wall
Outlet (P = 0)
Z
Y
X

Figure 1

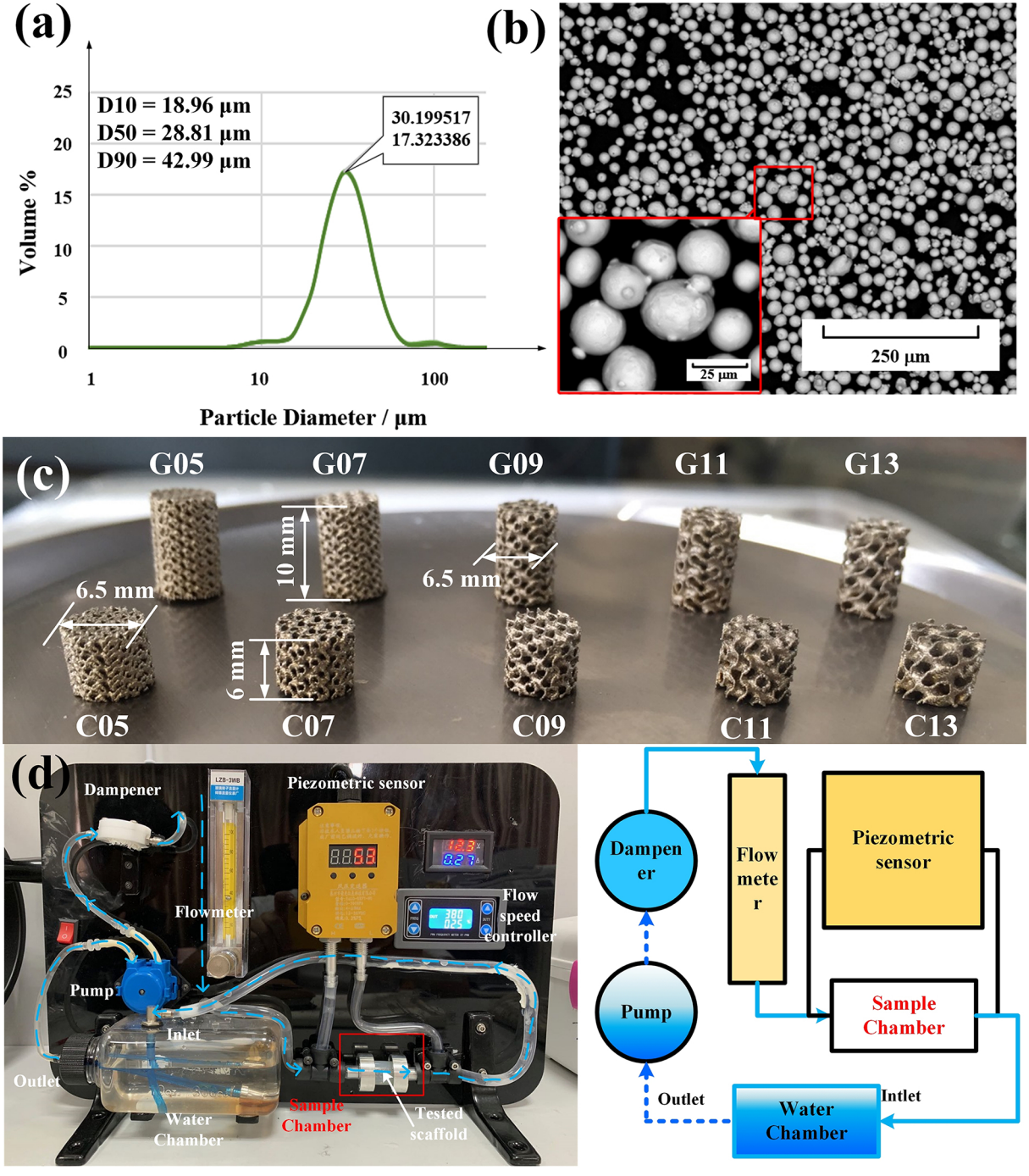
(a)
D10 = 18.96 µm
D50 = 28.81 µm
D90 = 42.99 µm
30.199517
17.323386
Volume %
Particle Diameter / µm
(b)
25 µm
250 µm
(c)
G05
G07
G09
G11
G13
6.5 mm
10 mm
6 mm
6.5 mm
C05
C07
C09
C11
C13
(d)
Dampener
Piezometric sensor
Flowmeter
Flow speed controller
Pump
Inlet
Outlet
Water Chamber
Sample Chamber
Tested scaffold
Dampener
Flow meter
Piezometric sensor
Pump
Sample Chamber
Outlet
Intlet
Water Chamber

Figure 2

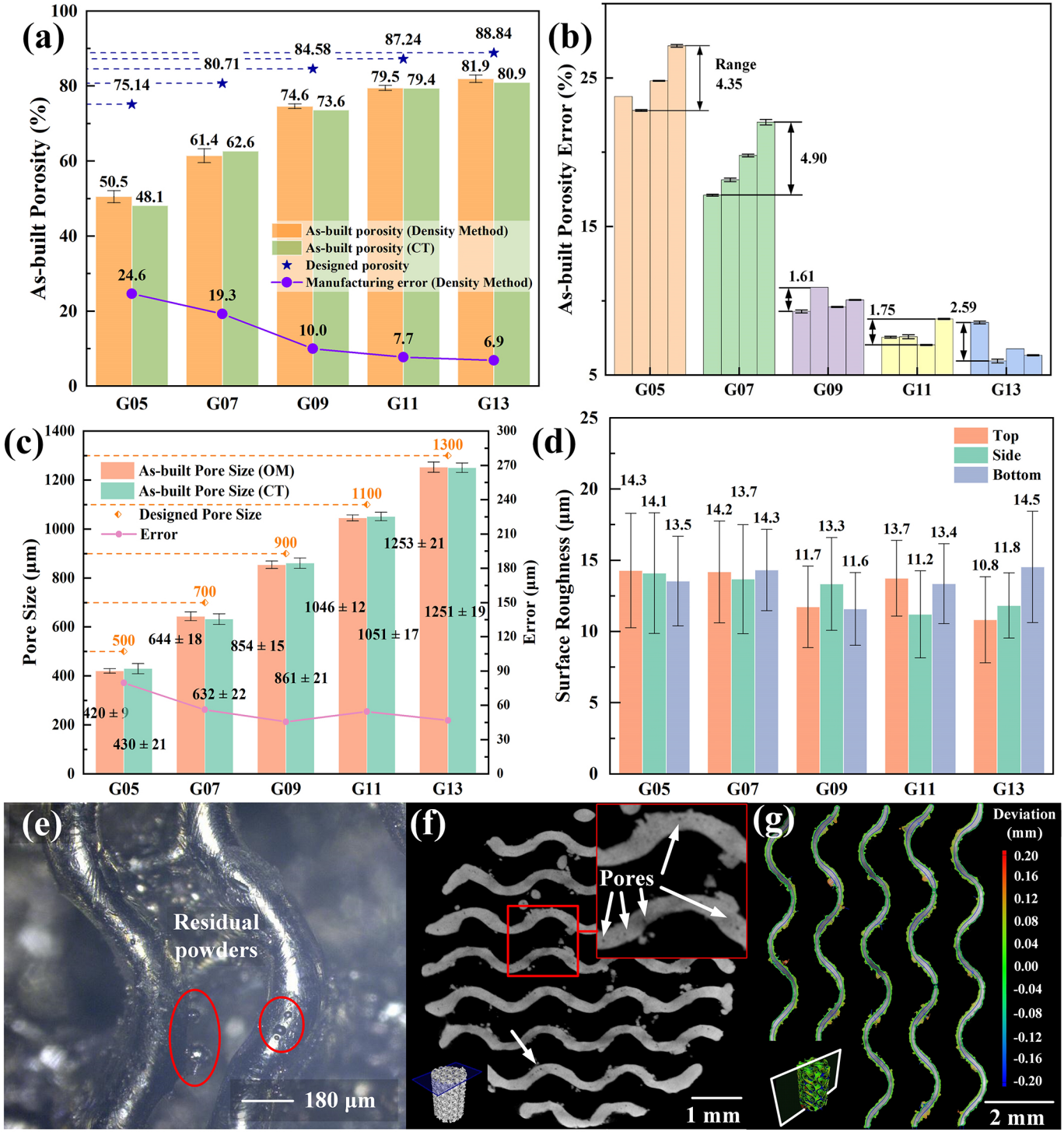
(a)
As-built Porosity (%)
100
80
60
40
20
0
75.14
80.71
84.58
87.24
88.84
50.5
48.1
61.4
62.6
74.6
73.6
79.5
79.4
81.9
80.9
24.6
19.3
10.0
7.7
6.9
G05
G07
G09
G11
G13
As-built porosity (Density Method)
As-built porosity (CT)
Designed porosity
Manufacturing error (Density Method)
(b)
As-built Porosity Error (%)
25
15
5
Range
4.35
4.90
1.61
1.75
2.59
G05
G07
G09
G11
G13
(c)
Pore Size (μm)
1400
1200
1000
800
600
400
200
0
Error (μm)
300
270
240
210
180
150
120
90
60
30
0
As-built Pore Size (OM)
As-built Pore Size (CT)
Designed Pore Size
Error
500
700
900
1100
1300
420 ± 9
430 ± 21
644 ± 18
632 ± 22
854 ± 15
861 ± 21
1046 ± 12
1051 ± 17
1253 ± 21
1251 ± 19
G05
G07
G09
G11
G13
(d)
Surface Roughness (μm)
25
20
15
10
5
0
Top
Side
Bottom
14.3
14.1
13.5
14.2
13.7
14.3
11.7
13.3
11.6
13.7
11.2
13.4
10.8
11.8
14.5
G05
G07
G09
G11
G13
(e)
Residual powders
180 μm
(f)
Pores
1 mm
(g)
Deviation (mm)
0.20
0.16
0.12
0.08
0.04
0.00
-0.04
-0.08
-0.12
-0.16
-0.20
2 mm

Figure 3

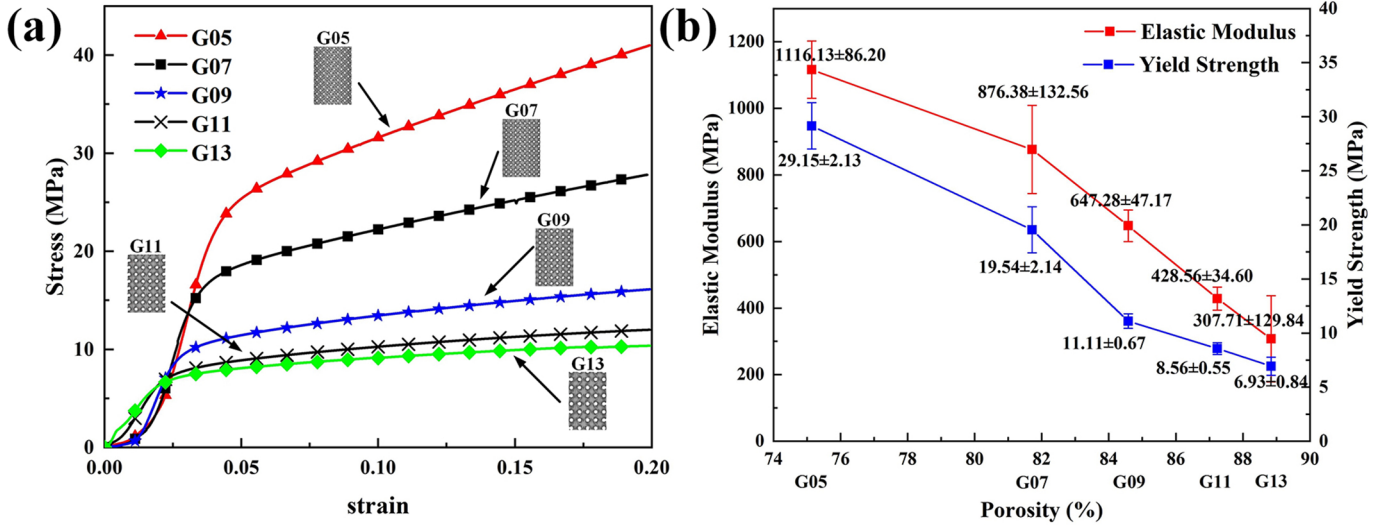
(a)
G05
G07
G09
G11
G13
Stress (MPa)
strain
0.00
0.05
0.10
0.15
0.20
0
10
20
30
40
(b)
Elastic Modulus
Yield Strength
1116.13±86.20
876.38±132.56
647.28±47.17
428.56±34.60
307.71±129.84
29.15±2.13
19.54±2.14
11.11±0.67
8.56±0.55
6.93±0.84
Elastic Modulus (MPa)
Yield Strength (MPa)
Porosity (%)
74
76
78
80
82
84
86
88
90
0
200
400
600
800
1000
1200
0
5
10
15
20
25
30
35
40
G05
G07
G09
G11
G13

Figure 4

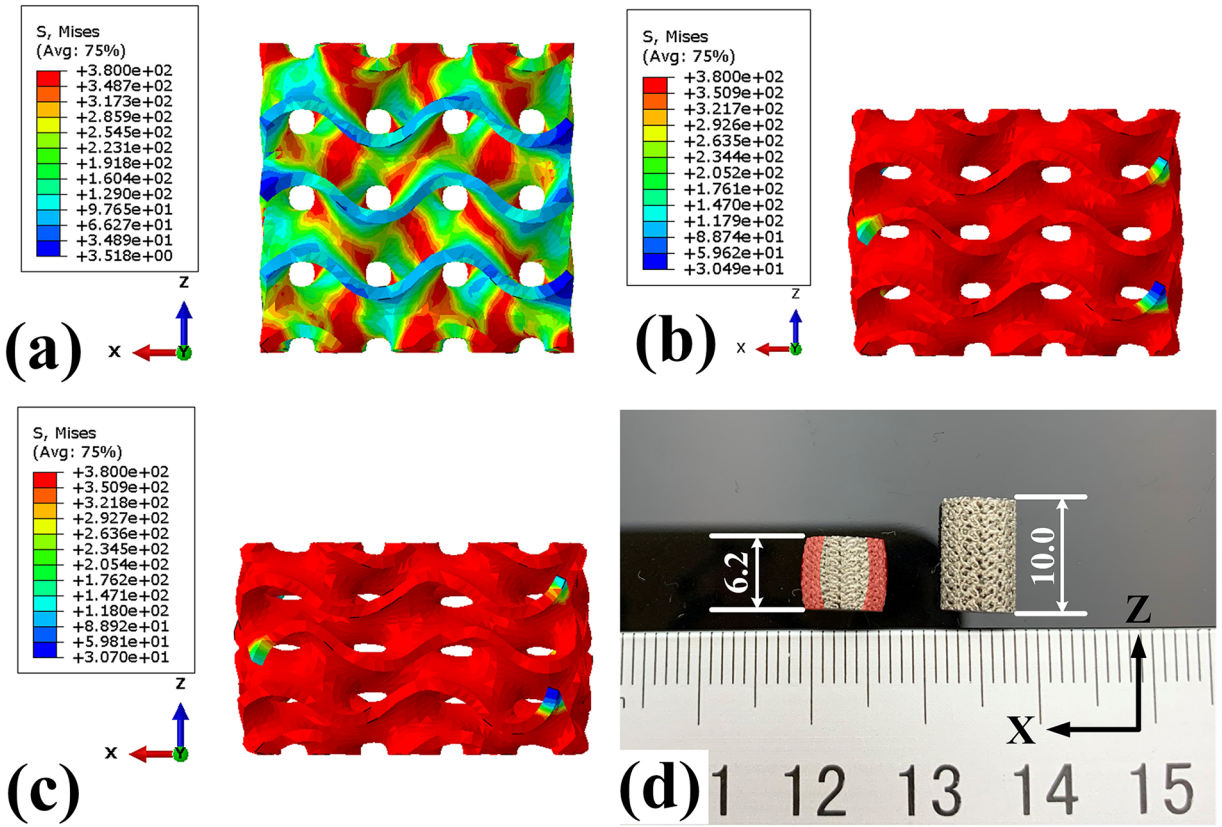
S, Mises
(Avg: 75%)
+3.800e+02
+3.487e+02
+3.173e+02
+2.859e+02
+2.545e+02
+2.231e+02
+1.918e+02
+1.604e+02
+1.290e+02
+9.765e+01
+6.627e+01
+3.489e+01
+3.518e+00
(a)
S, Mises
(Avg: 75%)
+3.800e+02
+3.509e+02
+3.217e+02
+2.926e+02
+2.635e+02
+2.344e+02
+2.052e+02
+1.761e+02
+1.470e+02
+1.179e+02
+8.874e+01
+5.962e+01
+3.049e+01
(b)
S, Mises
(Avg: 75%)
+3.800e+02
+3.509e+02
+3.218e+02
+2.927e+02
+2.636e+02
+2.345e+02
+2.054e+02
+1.762e+02
+1.471e+02
+1.180e+02
+8.892e+01
+5.981e+01
+3.070e+01
(c)
6.2
10.0
Z
X
(d)
1 12 13 14 15

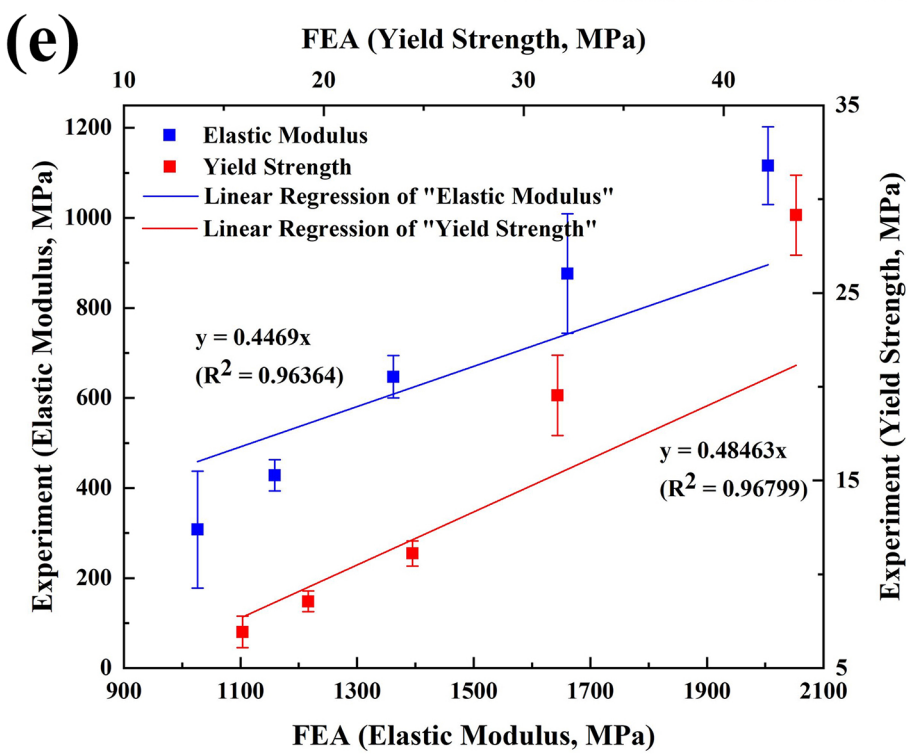
(e)
FEA (Yield Strength, MPa)
10
20
30
40
Elastic Modulus
Yield Strength
Linear Regression of "Elastic Modulus"
Linear Regression of "Yield Strength"
y = 0.4469x
(R2 = 0.96364)
y = 0.48463x
(R2 = 0.96799)
Experiment (Elastic Modulus, MPa)
0
200
400
600
800
1000
1200
Experiment (Yield Strength, MPa)
5
15
25
35
900
1100
1300
1500
1700
1900
2100
FEA (Elastic Modulus, MPa)

Figure 5

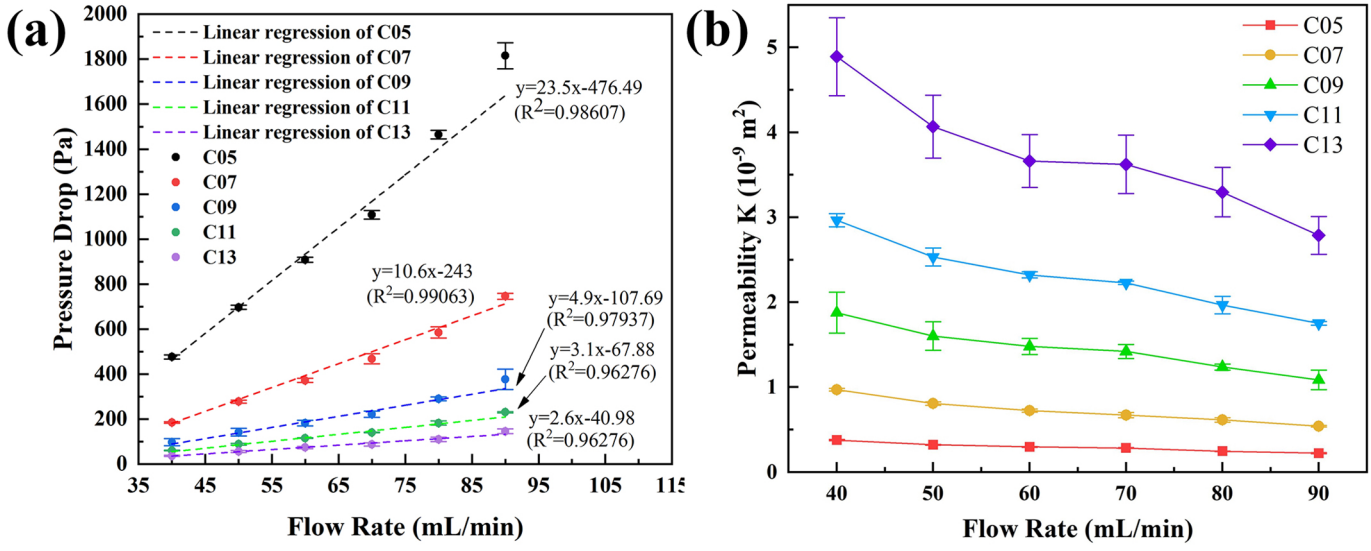
(a)
Linear regression of C05
Linear regression of C07
Linear regression of C09
Linear regression of C11
Linear regression of C13
C05
C07
C09
C11
C13
y=23.5x-476.49
(R2=0.98607)
y=10.6x-243
(R2=0.99063)
y=4.9x-107.69
(R2=0.97937)
y=3.1x-67.88
(R2=0.96276)
y=2.6x-40.98
(R2=0.96276)
Pressure Drop (Pa)
Flow Rate (mL/min)
(b)
C05
C07
C09
C11
C13
Permeability K (10-9 m2)
Flow Rate (mL/min)

Figure 6

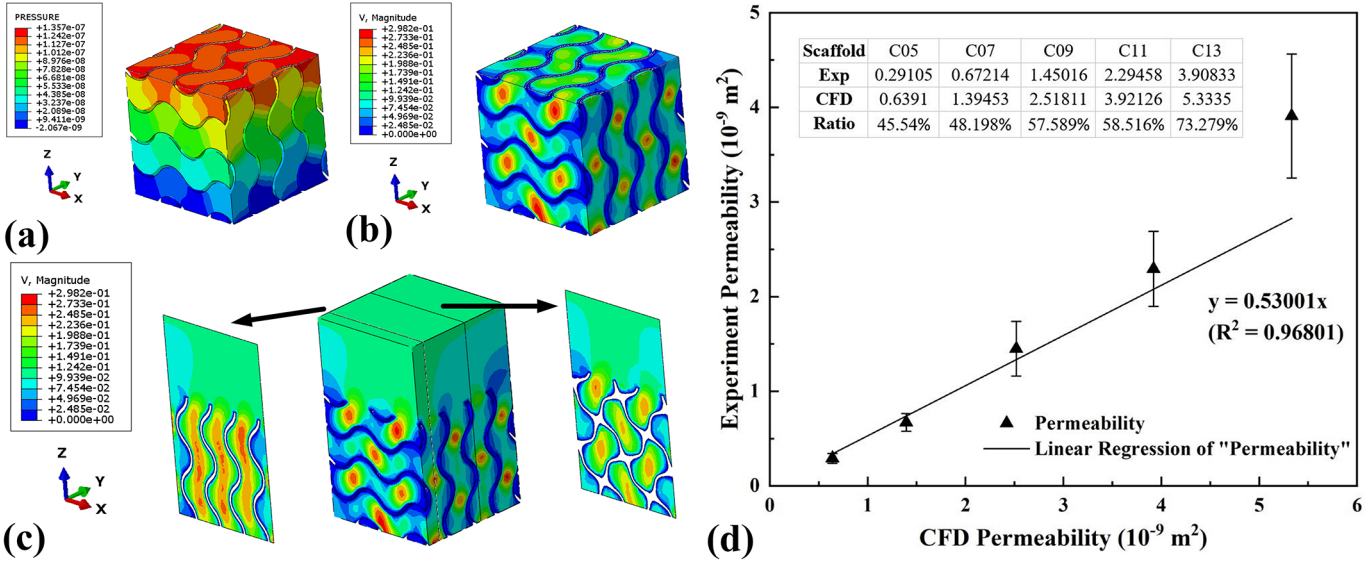
PRESSURE
+1.357e-07
+1.242e-07
+1.127e-07
+1.012e-07
+8.976e-08
+7.828e-08
+6.681e-08
+5.533e-08
+4.385e-08
+3.237e-08
+2.089e-08
+9.411e-09
-2.067e-09
Z
Y
X
(a)
V, Magnitude
+2.982e-01
+2.733e-01
+2.485e-01
+2.236e-01
+1.988e-01
+1.739e-01
+1.491e-01
+1.242e-01
+9.939e-02
+7.454e-02
+4.969e-02
+2.485e-02
+0.000e+00
Z
Y
X
(b)
V, Magnitude
+2.982e-01
+2.733e-01
+2.485e-01
+2.236e-01
+1.988e-01
+1.739e-01
+1.491e-01
+1.242e-01
+9.939e-02
+7.454e-02
+4.969e-02
+2.485e-02
+0.000e+00
Z
Y
X
(c)
Scaffold C05 C07 C09 C11 C13
Exp 0.29105 0.67214 1.45016 2.29458 3.90833
CFD 0.6391 1.39453 2.51811 3.92126 5.3335
Ratio 45.54% 48.198% 57.589% 58.516% 73.279%
Experiment Permeability (10-9 m2)
CFD Permeability (10-9 m2)
y = 0.53001x
(R2 = 0.96801)
Permeability
Linear Regression of "Permeability"
0
1
2
3
4
5
6
(d)

Figure 7

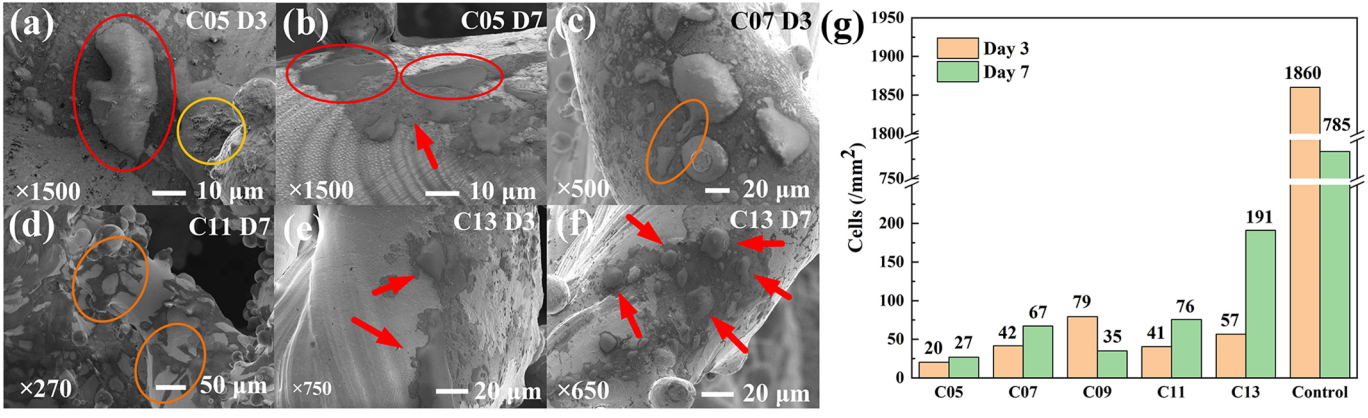
(a)
C05 D3
×1500
10 μm
(b)
C05 D7
×1500
10 μm
(c)
C07 D3
×500
20 μm
(d)
C11 D7
×270
50 μm
(e)
C13 D3
×750
20 μm
(f)
C13 D7
×650
20 μm
(g)
Day 3
Day 7
Cells (/mm²)
1950
1900
1850
1800
750
200
150
100
50
0
20
27
42
67
79
35
41
76
57
191
1860
785
C05
C07
C09
C11
C13
Control

Figure 8